



学位論文

Interaction between
Accretion Disk Penetrated by Large-scale Magnetic Field
and the Magnetosphere of Young Stellar Object

大局的磁場に貫かれた降着円盤と
形成中の星の磁気圏の相互作用

平成5年12月博士(理学)申請

東京大学大学院理学系研究科
天文学専攻
廣瀬 重信

①

学位論文

Interaction between
Accretion Disk Penetrated by Large-scale Magnetic Field
and the Magnetosphere of Young Stellar Object

大局的磁場に貫かれた降着円盤と
形成中の星の磁気圏の相互作用

平成5年12月博士（理学）申請

東京大学大学院理学系研究科
天文学専攻

廣瀬 重信

文部省

Interaction between
Accretion Disk Penetrated by Large-scale Magnetic Field
and the Magnetosphere of Young Stellar Object

大塚 隆夫
東京大学理学部天文学科

〒113 東京都文京区根津1-1-1

東京大学理学部天文学科

〒113

大塚 隆夫

Shigenobu Hirose

Interaction between
Accretion Disk Penetrated by Large-scale Magnetic field
and the Magnetosphere of Young Stellar Object

Shigenobu Hirose

Department of Astronomy
School of Science
University of Tokyo

24 December 1993

Interaction between
Accretion Disk Torques and Large-scale Magnetic Field
and the Magnetosphere of Young Stellar Objects

Shigeharu Hirano

Department of Astronomy,
School of Science,
University of Tokyo

38 December 1997

Abstract

Dedicated to my family

It is generally believed that the interaction between the accretion disk and the magnetosphere of a young star is a key to understanding the evolution of the star. In this paper, we study the interaction between the accretion disk and the magnetosphere of a young star, focusing on the role of the large-scale magnetic field. We show that the interaction between the accretion disk and the magnetosphere is strongly affected by the large-scale magnetic field. In particular, the interaction is significantly affected by the large-scale magnetic field in the case of a young star with a large-scale magnetic field. We show that the interaction between the accretion disk and the magnetosphere is significantly affected by the large-scale magnetic field in the case of a young star with a large-scale magnetic field. We show that the interaction between the accretion disk and the magnetosphere is significantly affected by the large-scale magnetic field in the case of a young star with a large-scale magnetic field.

We study the interaction between the accretion disk and the magnetosphere of a young star, focusing on the role of the large-scale magnetic field. We show that the interaction between the accretion disk and the magnetosphere is significantly affected by the large-scale magnetic field. In particular, the interaction is significantly affected by the large-scale magnetic field in the case of a young star with a large-scale magnetic field. We show that the interaction between the accretion disk and the magnetosphere is significantly affected by the large-scale magnetic field in the case of a young star with a large-scale magnetic field. We show that the interaction between the accretion disk and the magnetosphere is significantly affected by the large-scale magnetic field in the case of a young star with a large-scale magnetic field.

We study the interaction between the accretion disk and the magnetosphere of a young star, focusing on the role of the large-scale magnetic field. We show that the interaction between the accretion disk and the magnetosphere is significantly affected by the large-scale magnetic field. In particular, the interaction is significantly affected by the large-scale magnetic field in the case of a young star with a large-scale magnetic field. We show that the interaction between the accretion disk and the magnetosphere is significantly affected by the large-scale magnetic field in the case of a young star with a large-scale magnetic field. We show that the interaction between the accretion disk and the magnetosphere is significantly affected by the large-scale magnetic field in the case of a young star with a large-scale magnetic field.

Abstract

Outflow phenomena are ubiquitous in star forming regions. Observations suggest that there are three different classes of outflows emerging from the region of star formation. It became clear that all these three are closely related to the disk accretion process. In the present paper, we deal with the formation of one class of outflows, "optical jets", which are high-velocity and highly collimated jets. They are considered to be ejected from the vicinity of forming stars and thus to reflect the final accretion process.

We consider the scenario of the star formation as follows. As a result of the contraction of the gas cloud having a large-scale interstellar magnetic field in it, the central star formed at the center will possess a large amount of magnetic flux and attain its own magnetosphere with magnetic field of considerable strength. It will truncate the accretion disk which also carries a large-scale magnetic field in their contraction, at a distance of several stellar radii. Thus the final accretion and the acceleration of the optical jets are expected to be controlled by the magnetic action.

To study the interaction between the magnetized disk and the magnetosphere of the central star, we performed 2.5-dimensional Magnetohydrodynamics (MHD) simulations. (As a first step, we treat a case with no stellar rotation in this work.) We found that the final accretion onto the central star and the acceleration of a collimated jet occur through the magnetic reconnection at the magnetically neutral ring formed in the equatorial plane between the disk and the magnetosphere; The accretion disk presses on the magnetosphere by losing its angular momentum through the magnetic braking, and an energized magnetically neutral ring is created at the interface between the disk and the magnetosphere, and then magnetic reconnection takes place. The disk material is transferred to the magnetosphere through

the magnetic reconnection, and a large fraction of the disk material is magnetically braked further by the star and can accrete onto the central star. On the other hand, ten percent or so of the material, which is initially located near the disk surface, is ejected along the reconnected stellar field lines and forms collimated bipolar jets. The acceleration of the jets is due to the Lorentz force associated with the propagation of the relaxing distortion as finite amplitude MHD waves, generated through the magnetic reconnection in three dimensions. The ultimate source of the energy of the jet is the gravitational potential energy of the disk material, once stored in the form of the energy in the magnetic stress at the squeezed magnetically neutral ring.

In the case of a rotating star, the jets will be further accelerated magneto-centrifugally as the material coasts along the field lines by the stellar rotation out to the Alfvén radius, which in turn, means the angular momentum loss due to the formation of the jets. If the Alfvén radius has an appropriate value, the negative torque by the jet may cancel the positive torque by the disk accretion and may regulate the angular velocity of the central star.

In our extended model, we can explain the observed multiple-structured outflows in the star forming regions; We have a highly collimated jet from the interface between the disk and the magnetosphere of the star, and less collimated outflows from the surface of the surrounding disk penetrated by large-scale magnetic field. The former is due to the magnetic reconnection together with further magneto-centrifugal acceleration by the rotating star discussed above and may correspond to the optical jets, whereas the latter is accelerated by the magnetic actions including the relaxation of the gradient of the toroidal magnetic pressure produced by the disk rotation as well as the magneto-centrifugal force. The latter coming from the inner

part of the disk with energetic rotation and strong magnetic field may explain the so-called "high-velocity neutral winds", while the latter from the extended external region of the disk may correspond to the large-scale molecular bipolar outflows. The angular momentum loss by the formation of the collimated jet, that is, the optical jet, along the stellar open fields may explain the relatively low and constant rotation rate of the T Tauri stars in the phase of disk accretion.

Contents

Abstract	1
Contents	4
Chapter 1 Introduction	6
1.1 Energetic Outflows from Young Stellar Objects	6
1.1.1 Multiple Structures of Outflows	6
1.1.2 Outflows Driven by Disk Accretion	8
1.1.3 Models for Outflow Phenomena Proposed Thus-far	10
1.2 Situation of Our Model to be Proposed	12
1.2.1 Star Formation from the Interstellar Cloud	12
having a Large-scale Magnetic Field	12
1.2.2 Final Accretion onto the Magnetized YSO	15
from the Disk having a Large-scale Magnetic Field	15
Chapter 2 Basic Equations and Numerical Method	17
2.1 Basic Equations	17
2.2 Numerical Method	18
2.2.1 Scalar Conservation Form of MHD Equations	18
2.2.2 Modified Lax-Wendroff Scheme with Artificial Viscosity	19
2.2.3 Lorentz-Force Term in the Equation of Motion	21
2.3 Dimensionless Equation System	22
2.4 Initial Conditions and Dimensionless Parameters	23
2.4.1 Initial Conditions	23
2.4.2 Dimensionless Parameters	24
2.5 Simulation Region and Boundary Conditions	26
2.5.1 Boundary Conditions at Outer Boundaries,	26
r-axis and z-axis	26
2.5.2 Boundary Condition at the Stellar Surface	28

2.6 Resistivity Model	30
Chapter 3 Numerical Results	32
3.1 Physical Parameters and Outline of the Results	32
3.2 Disk Accretion by Magnetic Braking	34
3.3 Driven Reconnection by Disk Accretion	35
3.4 Mass and Angular Momentum Transfer	37
through Magnetic Reconnection	37
3.5 Acceleration of Collimated Jet	41
Associated with MHD Wave Propagation	41
3.6 The Case of High-Density Disk	44
Chapter 4 Discussion	47
4.1 The Effect of the Stellar Rotation	47
4.1.1 Qualitative Behavior of the System	48
in the Case of a Rotating Star	48
4.1.2 The Effect on the Angular Momentum Transfer	50
4.1.3 The Effect on the Acceleration of the jet	52
4.1.4 Summary of the Effect of the Stellar Rotation	52
4.2 Applications to the YSO-related Phenomena	53
4.2.1 Outflows from YSOs	54
4.2.2 Angular Momentum Problem	58
Chapter 5 Summary and Overall Discussion	62
- The Dynamical Role of Magnetic Fields	62
- in the Whole Star Formation Process -	62
References	67

Chapter 1

Introduction

1.1 Energetic Outflows from Young Stellar Objects

Energetic outflows are ubiquitous phenomena with young stellar objects (YSOs) which are considered to be in the disk accretion phase, ranging from protostars (which are here defined as deeply embedded infrared sources) to Classical T Tauri Stars (CTTSs). The outflow phenomena are very important in the sense that they reflect the accretion process in the star formation and that they are also the key to the cease of accretion and the mass partition between the central star and the surrounding disk (Shu and Terebey 1984, Shu et al. 1987).

1.1.1 Multiple Structure of Outflows

First, we summarize the characteristics of the outflow phenomena. In the stage of the protostar, three types of outflows have been found, (i) molecular bipolar outflows, (ii) optical jets, and (iii) high-velocity neutral winds. They differ in the characteristic scale, velocity, degree of collimation and so on. (See Table 1.1 and Figure 1.1(a).)

Molecular bipolar outflows observed in millimetric CO lines (Snell et al. 1980;

see reviews Lada 1985, Fukui et al. 1993) have a characteristic scale of ~ 1 pc and velocity of ~ 20 kms $^{-1}$, and are most loosely collimated among these three. Its kinetic luminosity is about hundred times smaller than the stellar luminosity which is explained as the released gravitational energy, but its momentum discharge is about hundred times larger than radiative momentum discharge, which shows that it can not be driven by the radiation pressure.

Optical jets observed in optical forbidden lines [OI] or [SII] (Mundt and Fried 1983, Mundt et al. 1987) are high-velocity and highly collimated jets, and are considered to be ejected from the closer vicinity of the central star. They show similar spectroscopic properties to Herbig-Haro objects (HH objects), and it is considered lately that HH objects are actually related to optical jets ejected from YSOs. The typical velocity of optical jets is $200 \sim 400$ kms $^{-1}$ and the typical scale is $0.05 \sim 0.1$ pc. Their momentum discharge is much smaller than that of the molecular outflows, but it is still larger than the radiative momentum discharge of the star. One of the characteristics of optical jets is their temporal variability or non-steady outflow episodes (Reipurth 1989, Mitchell et al. 1988a, Raga et al. 1990, Mundt et al. 1987, 1990), which may give some restrictions to their mechanism of formation.

High-velocity neutral winds have been found in the last several years by using HI and CO lines (Lizano et al. 1988, Koo 1989, 1990, Mitchell et al. 1988b, 1989). Their typical velocity is a few hundred kms $^{-1}$ and the degree of collimation is roughly between those of molecular bipolar outflows and optical jets. Since they have momentum discharge comparable to that of molecular bipolar outflows and have kinetic luminosities larger than that of molecular bipolar outflows, some people think that large-scale molecular bipolar outflows are the shells swept up by high-velocity neutral winds.

Three types of outflows above are also observed in CTTS phase, at least in its early stage (Edwards and Snell 1982, Calvet et al. 1983, Edwards et al. 1993). On the other hands, from the profile of forbidden lines [OI] or S[II], it had been considered that there exist energetic wind from the central star in CTTS phase (so-called "T Tauri wind"). But recent high spectral resolution observations suggest that they are hollow rather than spherical (Appenzeller et al. 1984, Edwards et al. 1987), or that they consist of two separate gas components (Kwan and Tademaru 1988). Anyway it is now considered that T Tauri winds are not spherical stellar winds and that forbidden line emissions may originate from the part of outflows which are not resolved (< 100 AU) (Pudritz et al. 1991, Edwards et al. 1993a).

1.1.2 Outflows Driven by Disk Accretion

Recent observations suggest that there exist small scale ($10^2 \sim 10^3$ AU) circumstellar disks around YSOs both in the stage of protostar and in the stage of CTTS. It has been remarked that the large infrared excesses of the spectral energy distributions of these systems show indirect evidence for the presence of circumstellar disks (Adams et al. 1987). Forbidden line profiles of CTTSs show preferentially blue-shifted wings, suggesting the presence of optically thick disk which occults the red-shifted component (Appenzeller 1983). Now, direct images are obtained for a few sources by molecular line and millimeter continuum interferometric observations (Sargent and Beckwith 1987, 1991, Hayashi et al. 1993). It is considered that these circumstellar disk are in the state of accretion and the final accretion onto YSO are occurring from the inner edge of the disks.

There is growing evidence that outflows are driven by the disk accretion. First,

the observed surrogate diagnostic for the mass loss rate by the outflow \dot{M}_o correlates with that for the mass accretion rate in the disk \dot{M}_{acc} , for all types of outflows. (Lada 1985, Cabrit et al. 1990, Levreault 1988, Edwards et al. 1993a). Another fact which indicates that the disk accretion, not the central star itself, may be driving outflows is the comparison of CTTSs with weak line T Tauri stars (WTTs). WTTs have almost same stellar properties (such as the internal structure or rotational period) as CTTSs, but show no evidence of energetic outflows and circumstellar disks in the state of accretion.

Now we can summarize the outflow phenomena in YSOs as follows. There is an intrinsically multiple system of outflows which are closely related with the disk accretion process. They are highly collimated optical jets, outer extended high-velocity neutral winds and surrounding large-scale molecular bipolar outflows. From energetic point of view, collimated optical jet and extended high-velocity neutral wind which have characteristic velocities of a few hundred kms^{-1} may be formed deep in the gravitational well, in the vicinity of the central star, while molecular bipolar outflows whose velocity is a few tens of kms^{-1} may be formed in the outer region, if we adopt the idea that their energy source is the released gravitational energy of the accreting material, as discussed above. The basic characteristics of outflows, such as the kinetic luminosity or the momentum discharge, are nearly the same in both protostars and CTTSs. (In the later stage of CTTSs, optical jets and molecular bipolar outflows are not observed apparently. But this does not necessarily mean that these outflows are not actually formed, because the appearance of them may depend on the amount of the outflow gas (and thus, the accretion rate) or the condition of the ambient medium into which outflows are injected.)

1.1.3 Models for Outflow Phenomena Proposed Thus-far

Various models are proposed to explain extended molecular bipolar outflows or high-velocity neutral winds. One of the stellar origin models is that they are driven by shear MHD waves generated in the convection zone (DeCampi 1981, Hartmann et al. 1982, Lago 1984), and another idea was proposed by Draine (1983) or Hartmann and MacGregor (1982), who considered winds driven by the stellar rotation through the magnetic action. Pudritz and Norman (1983, 1986) proposed a steady magneto-centrifugally driven wind (CDW) from accretion disks around YSOs. Königl (1989) also proposed a steady CDW model, which, in contrast, is self-consistent against the shearing and radial advection of magnetic fields, introducing field diffusion. Uchida and Shibata (1985), on the other hand, gave an MHD model in which the twisting up of the large-scale magnetic field and the relaxation of it into the bipolar directions accelerates the outflows. Their MHD simulation demonstrated that the "sweeping pinch" effect and also the centrifugal driving process act in a self-consistent way. Lovelace et al. (1991) proposed steady magnetic pressure-driven winds from the accretion disk, starting from the Uchida and Shibata (1985)'s idea. Shu et al. (1988) or Camenzind (1990) considered the steady CDW along the stellar open fields from the boundary between the magnetized star and the disk.

On the other hand, the origin of the collimated optical jet has not been very much discussed compared with the extended outflows, because their physical parameters are not yet determined precisely. Uchida and Shibata (1984) proposed the "polar crown-accretion shock" model. They assumed a non-rotating gaseous nebula in magnetohydrostatic equilibrium which is penetrated by large-scale magnetic field around the central star which possesses a dipolar magnetosphere (Uchida and Low 1981). The nebula mass enters the magnetosphere through the magnetic re-

connection at the magnetically neutral ring in the equatorial plane, and accretes onto the stellar polar crown along the magnetospheric field lines. They performed 1.5-dimensional adiabatic MHD simulations, showing that the recoiled shock blows off the tail of the accreting material to form a collimated jet along the field lines which have been converted from closed equatorial stellar fields to open stellar polar fields through the magnetic reconnection. There may also be a possibility that the collimated jet is driven by thermal pressure (Torbett 1984) or toroidal magnetic pressure (Pringle 1989), generated by the velocity shear at the boundary layer between the star and the circumstellar disk. Another way to form the collimated jet is to collimate the otherwise isotropic stellar wind in some way, for example, by outflows from the outer region (Shu et al. 1988) or by the gas pressure of ambient medium (Königl 1982, Raga and Canto 1989).

Although many ideas have been proposed for outflow phenomena as discussed above, most of them agree that outflows are powered by the rotation of the accretion disk (or the central star) through open magnetic fields, and their origin is the accretion disk itself or the boundary between the central star and the accretion disk, rather than the central star itself. Open magnetic fields will also contribute to the collimation of outflows. Some observations actually suggest the importance of the magnetic fields in the outflow phenomena. Uchida et al. (1987a, 1987b) found the spinning of the molecular bipolar outflow in L1551, which will be the result of the interaction between the accretion disk and the outflow through the open magnetic fields penetrating the disk (Uchida and Shibata 1985). From the polarization measurements, Strom et al. (1986) showed that most of molecular bipolar outflows and the associated jets are almost parallel with ambient magnetic fields.

1.2 Situation of Our Model to be Proposed

As discussed in the previous sections, it is now considered that both the disk accretion and the magnetic field will play important roles on the formation of outflows. Now we must construct a unified model of the accretion process which explain outflows with the multiple structure in a self-consistent way, taking account of the actions of magnetic fields. Also the origin of the magnetic fields must be clarified at the same time.

In the present paper, we consider the accretion process in YSOs following the scenario of the star formation from the interstellar cloud penetrated by a large-scale magnetic fields, and try to explain the outflow phenomena and other YSO-related problems. We especially concentrate on the final accretion process onto the magnetized YSO and its related phenomena, which has not yet been studied completely (Uchida and Shibata 1984). We performed 2.5-dimensional MHD simulations and found a new regime of the mechanism of the formation of collimated jets, which is associated with the magnetic reconnection at the interface between the magnetosphere and the disk penetrated by a large-scale magnetic field. We consider that this "reconnection-driven jet" will correspond to the optical jets.

1.2.1 Star Formation from the Interstellar Cloud having a Large-scale Magnetic Field

First we consider the scenario of the star formation from the interstellar cloud having a large-scale magnetic field (Uchida and Shibata 1984, 1985).

Although the large portion of the magnetic flux will be reduced in the contraction of the cloud through the ambipolar diffusion or the Ohmic diffusion, a signifi-

cant amount of magnetic flux will be taken into the stellar core, and the central star will get a dipolar magnetosphere (Nakano and Umebayashi 1986). The magnetized central star will accrete the material from the circumstellar disk around it whose rotational axis is roughly parallel with the large-scale magnetic field, because the angular momentum component normal to the magnetic field will be preferentially removed from the contracting gas by causing escaping shear Alfvén waves in the early phase (Mestel 1965, Mouschovias and Paleologou 1980). Therefore, we hereafter assume that the magnetized central star is an aligned rotator for simplicity.

The frozen-in condition will be held and the disk will interact with the magnetic fields at least in the outer region where the surface density of the disk is low ($\geq 10 \sim 100$ AU) and in the inner region where the radiation from the central star is important ($\leq \sim 0.01$ AU) (Umebayashi and Nakano 1988, Nakano 1991). In the deep interior of the disk in between where the surface density is high and the temperature is low, the frozen-in condition may not be too good an approximation. But even in this range of the disk, the large-scale magnetic field will be penetrating the disk, because the large-scale magnetic field at the outer radius of the range which is convected from the outer region by disk accretion, will diffuse in and the field configuration will be force-free (or nearly uniform) (cf. Nakano and Umebayashi 1986). The magnetic field will recouple with the gas at the inner radius of the range and then will be convected toward the central star again by the disk accretion. Thus we may consider that the accretion disk will be penetrated by the large-scale magnetic field in the whole region, and the magnetic field in the outer region will be smoothly convected to the vicinity of the central star by the disk accretion, together with the magnetic diffusion in the decoupled region, if ever.

Nakano and Umebayashi (1986) estimated the magnetic field strength of a new-

born star as the order of thousand gauss at the pole. The magnetosphere of that strength will truncate the accretion disk at a distance of several stellar radii, which can be estimated as was done in the case of the disk accretion onto a magnetized neutron star (Pringle and Rees 1972, Ghosh and Lamb 1979, Arons 1993). (The large-scale magnetic field penetrating the disk in our case will not change markedly their argument of no disk-field case, because the disk field is assumed to be weak enough to be passive to the motion of the disk material.) At the inner edge of the disk, the stress of the accreting material will balance the magnetic stress of the magnetospheric field. Then we have the expression for the radius of the inner edge of the disk r_m ,

$$\frac{r_m}{R_*} = \alpha_t \left(\frac{B_*^4 R_*^2}{GM_* \dot{M}_{acc}} \right)^{\frac{1}{4}} \quad (\alpha_t \sim 0.5). \quad (1)$$

If we adopt typical values for the case of YSOs ($B_* \sim 10^{3.5}$ G, $R_* \sim 10^{11.5}$ cm, $M_* \sim 10^{33}$ g, $\dot{M}_{acc} \sim 10^{-7} M_{\odot} \text{yr}^{-1}$), we get several stellar radii for the radius of the inner edge of the disk.

In fact, recent X-ray and VLBI observations suggest that YSOs have ordered magnetic fields with the scale of several stellar radii and the strength of a few kilogauss at the stellar surface (see review Montmerle et al. 1993). The idea that the origin of the magnetism of YSOs is the dynamo action in the convective zone of the star (Shu et al. 1988) may be true in the later phase, but it is not likely in the earlier phase since YSOs are fully convective. Moreover there is evidence that a massive YSO which will not have a surface convective layer also has a magnetosphere (André et al. 1991). This suggests that the magnetic field in YSOs may be a fossil field brought into the star in the contraction from the interstellar gas with a weak magnetic field.

1.2.2 Final Accretion onto the Magnetized YSO from the Disk having a Large-scale Magnetic Field

Here we consider the interaction between the magnetosphere of the YSO and the disk penetrated by a large-scale magnetic field in the final accretion process (Figure 1.1(b)).

Since the large-scale magnetic field carried into the accretion disk and the dipolar field of the star are originated from the same interstellar field, the dipole moment of the star and the disk field are in the same direction, and a magnetically neutral ring is formed in the equatorial plane (Strittmatter 1965, Uchida and Shibata 1984, Nakano and Umebayashi 1986).

In this case, the magnetically neutral ring coincides with the inner edge of the disk. Thus the final accreting process, such as the mass and angular momentum transfer from the disk to the magnetosphere, will be controlled by the magnetic reconnection between the magnetospheric field and the disk field. We consider that the disk accretion drives the magnetic reconnection by building up a current at the neutral ring, which induces some kind of current-driven instability and thus the anomalous resistivity (see section 2.6).

The disk material transferred to the magnetosphere through magnetic reconnection will be funneled by the magnetospheric fields and fall toward the polar crown, if the radius of the inner edge of the disk is smaller than the corotation radius r_c , because the disk material is synchronized with the stellar rotation and thus become sub-Keplerian. At the corotation radius r_c , the rotational velocity of the Keplerian disk coincides with that of the magnetosphere rigidly rotating with the

stellar angular velocity Ω_* , which is expressed as follows.

$$\frac{r_c}{R_*} = \left(\frac{GM_*}{R_*^3 \Omega_*^2} \right)^{\frac{1}{2}} = \left(\frac{GM_*}{v_*^2 R_*} \right)^{\frac{1}{2}}, \quad (2)$$

where v_* is the surface velocity of the stellar rotation. In the T Tauri phase ($v_* \sim 20$ kms $^{-1}$), the corotation radius r_c is also several stellar radii. Hereafter we consider the case in which the corotation radius is larger than the inner edge of the disk for simplicity.

We performed 2.5-dimensional MHD simulations to study the process of the final accretion onto magnetized YSOs from the accretion disk with a large-scale magnetic field, because it is a highly non-linear process including the mass and angular momentum transfer from the disk to the magnetosphere controlled by the magnetic reconnection. We mainly demonstrated in the simulations the formation of collimated jets associated with the final accretion process, which will correspond to the optical jets. A unified model of outflows including other classes of outflows will be discussed in section 4. For the computational simplification, we deal as a first step, with the case in which the central star is not rotating. The discussion on the effect of the stellar rotation will also be given in section 4.

We structure the present paper as follows: In section 2, we present the basic equations and the numerical methods, and in section 3, we give the results of the simulations. Applications of our model to YSO-related phenomena will be discussed in section 4. Finally we give the summary and overall discussion in section 5, where the dynamical role of the magnetic field in the star formation process will be discussed.

Chapter 2

Basic Equations and Numerical Method

2.1 Basic Equations

We use the following system of MHD equations in which the resistive effect is taken into account. (We adopt the cgs emu.)

$$\frac{\partial \rho}{\partial t} + \nabla \cdot (\rho \mathbf{v}) = 0, \quad (1)$$

$$\rho \left[\frac{\partial \mathbf{v}}{\partial t} + (\mathbf{v} \cdot \nabla) \mathbf{v} \right] + \nabla p - \mathbf{j} \times \mathbf{B} - \rho \mathbf{g} = 0, \quad (2)$$

$$\frac{\partial \mathbf{B}}{\partial t} + \nabla \times (-\mathbf{v} \times \mathbf{B} + \eta \mathbf{j}) = 0, \quad (3)$$

$$\left[\frac{\partial}{\partial t} + (\mathbf{v} \cdot \nabla) \right] (\rho \rho^{-\gamma}) = 0, \quad (4)$$

$$\mathbf{j} = \frac{1}{4\pi} \nabla \times \mathbf{B}, \quad (5)$$

where η is the electrical resistivity (the formulation is given in section 2.6), and γ is the adiabatic exponent. Adiabatic approximation is used for the energy equation.

2.2 Numerical Method

2.2.1 Scalar Conservation Form of MHD Equations

We adopt a cylindrical coordinate system (r, ϕ, z) , assuming axisymmetry around the z -axis, but allowing the ϕ components of vector quantities \mathbf{v} and \mathbf{B} (so-called 2.5-dimensional formulation), which are intrinsically important in our case. Then the resistive MHD equations (1)~(5) can be written in the scalar conservation form as follows:

$$\frac{\partial \rho}{\partial t} + \frac{\partial}{\partial r}(\rho v_r) + \frac{\partial}{\partial z}(\rho v_z) + \frac{\rho v_r}{r} = 0, \quad (6)$$

$$\begin{aligned} \frac{\partial}{\partial t}(\rho v_r) + \frac{\partial}{\partial r} \left[\rho v_r^2 + p + \frac{1}{8\pi} (B_z^2 + B_\phi^2 - B_r^2) \right] \\ + \frac{\partial}{\partial z}(\rho v_r v_z - \frac{1}{4\pi} B_r B_z) + \frac{1}{r} \left[\rho (v_r^2 - v_\phi^2) + \frac{1}{4\pi} (B_\phi^2 - B_r^2) \right] + \rho g_r = 0, \end{aligned} \quad (7)$$

$$\begin{aligned} \frac{\partial}{\partial t}(\rho v_\phi) + \frac{\partial}{\partial r}(\rho v_r v_\phi - \frac{1}{4\pi} B_r B_\phi) \\ + \frac{\partial}{\partial z}(\rho v_z v_\phi - \frac{1}{4\pi} B_z B_\phi) + \frac{2}{r}(\rho v_r v_\phi - \frac{1}{4\pi} B_r B_\phi) = 0, \end{aligned} \quad (8)$$

$$\begin{aligned} \frac{\partial}{\partial t}(\rho v_z) + \frac{\partial}{\partial r}(\rho v_r v_z - \frac{1}{4\pi} B_r B_z) \\ + \frac{\partial}{\partial z} \left[\rho v_z^2 + p + \frac{1}{8\pi} (B_z^2 + B_\phi^2 - B_r^2) \right] + \frac{1}{r}(\rho v_r v_z - \frac{1}{4\pi} B_r B_z) + \rho g_z = 0, \end{aligned} \quad (9)$$

$$\frac{\partial B_r}{\partial t} + \frac{\partial}{\partial z}(v_z B_r - v_r B_z - \eta j_\phi) = 0, \quad (10)$$

$$\frac{\partial B_\phi}{\partial t} + \frac{\partial}{\partial r}(v_r B_\phi - v_\phi B_r - \eta j_z) - \frac{\partial}{\partial z}(v_\phi B_z - v_z B_\phi - \eta j_r) = 0, \quad (11)$$

$$\frac{\partial B_z}{\partial t} - \frac{\partial}{\partial r}(v_z B_r - v_r B_z - \eta j_\phi) - \frac{1}{r}(v_r B_r - v_r B_z - \eta j_\phi) = 0, \quad (12)$$

$$\begin{aligned} \frac{\partial}{\partial t} \left(\frac{1}{\gamma-1} p + \frac{1}{2} \rho v^2 + \frac{1}{8\pi} B^2 \right) \\ + \frac{\partial}{\partial r} \left[\frac{\gamma}{\gamma-1} p v_r + \frac{1}{2} \rho v^2 v_r + \frac{1}{4\pi} B_z (v_r B_z - v_z B_r + \eta j_\phi) + \frac{1}{4\pi} B_\phi (v_r B_\phi - v_\phi B_r - \eta j_z) \right] \\ + \frac{\partial}{\partial z} \left[\frac{\gamma}{\gamma-1} p v_z + \frac{1}{2} \rho v^2 v_z + \frac{1}{4\pi} B_r (v_z B_r - v_r B_z - \eta j_\phi) + \frac{1}{4\pi} B_\phi (v_z B_\phi - v_\phi B_z - \eta j_r) \right] \\ + \frac{1}{r} \left[\frac{\gamma}{\gamma-1} p v_r + \frac{1}{2} \rho v^2 v_r + \frac{1}{4\pi} B_z (v_r B_z - v_z B_r + \eta j_\phi) + \frac{1}{4\pi} B_\phi (v_r B_\phi - v_\phi B_r - \eta j_z) \right] \end{aligned}$$

$$+ \rho(g_r v_r + g_z v_z) = 0. \quad (13)$$

2.2.2 Modified Lax-Wendroff Scheme with Artificial Viscosity

Each of the equations in the conservation forms (6)~(13) are generally expressed in the form,

$$\frac{\partial W}{\partial t} + \frac{\partial}{\partial r} F(W) + \frac{\partial}{\partial z} G(W) + S(W) = 0. \quad (14)$$

We solve the set of differential equations of the form (14) numerically with a finite difference method. We will indicate by $W_{i,j}^n$ the values of the function $W(r, z; t)$ at the discrete mesh points (r_i, z_j) and at the discrete time t_n . We adopt the variable meshes, that is, mesh sizes $\Delta r_i \equiv r_{i+1} - r_i$ and $\Delta z_j \equiv z_{j+1} - z_j$ are variable with r_i and z_j .

By applying Modified Lax-Wendroff scheme by Rubin and Burstein (1967), we obtain values at the time t_{n+1} from those at the time t_n in two steps as follows. First step :

$$\begin{aligned} \bar{W}_{i+\frac{1}{2}, j+\frac{1}{2}}^{n+1} = \frac{1}{4} \left(W_{i+1, j+1}^n + W_{i+1, j}^n + W_{i, j+1}^n + W_{i, j}^n \right) \\ - \frac{\Delta t}{2\Delta r_i} \left(F_{i+1, j+1}^n - F_{i, j+1}^n + F_{i+1, j}^n - F_{i, j}^n \right) \\ - \frac{\Delta t}{2\Delta z_j} \left(G_{i+1, j+1}^n - G_{i+1, j}^n + G_{i, j+1}^n - G_{i, j}^n \right) \\ - \frac{\Delta t}{4} \left(S_{i+1, j+1}^n + S_{i+1, j}^n + S_{i, j+1}^n + S_{i, j}^n \right) \end{aligned} \quad (15)$$

Second step :

$$W_{i,j}^{n+1} = W_{i,j}^n - \frac{\Delta t}{2\Delta r} \left(\frac{F_{i+1,j}^n - F_{i-1,j}^n}{2} + \bar{F}_{i+\frac{1}{2},j}^{n+1} - \bar{F}_{i-\frac{1}{2},j}^{n+1} \right) - \frac{\Delta t}{2\Delta z} \left(\frac{G_{i,j+1}^n - G_{i,j-1}^n}{2} + \bar{G}_{i,j+\frac{1}{2}}^{n+1} - \bar{G}_{i,j-\frac{1}{2}}^{n+1} \right) - \Delta t S_{i,j}^n, \quad (16)$$

where

$$\bar{F}_{i+\frac{1}{2},j}^{n+1} = \frac{\Delta z_{j-1}}{2\Delta z} F_{i+\frac{1}{2},j+\frac{1}{2}}^{n+1} + \frac{\Delta z_j}{2\Delta z} F_{i+\frac{1}{2},j-\frac{1}{2}}^{n+1},$$

$$\bar{G}_{i,j+\frac{1}{2}}^{n+1} = \frac{\Delta r_{i-1}}{2\Delta r} G_{i+\frac{1}{2},j+\frac{1}{2}}^{n+1} + \frac{\Delta r_i}{2\Delta r} G_{i-\frac{1}{2},j+\frac{1}{2}}^{n+1},$$

in which

$$\Delta r = (\Delta r_i + \Delta r_{i-1})/2, \quad \Delta z = (\Delta z_j + \Delta z_{j-1})/2.$$

The time step $\Delta t \equiv t_{n+1} - t_n$ is determined by Courant-Friedrichs-Lewy (CFL) condition :

$$\Delta t \leq \Delta t_{CFL} \equiv \frac{\min(\Delta r, \Delta z)}{\sqrt{v^2 + c_s^2 + v_A^2}}, \quad (17)$$

where v , c_s and v_A are the fluid velocity, the sound velocity and the Alfvénic velocity, respectively. We adopt $\Delta t = 0.4 \Delta t_{CFL}$.

To perform calculations stably, we add the following artificial viscosity term $Q_{i,j}^n$ (Richtmyer and Morton 1967) after the second step.

$$W_{i,j}^{n+1} = W_{i,j}^{n+1} + Q_{i,j}^{n+1}, \quad (18)$$

where

$$Q_{i,j}^{n+1} = \frac{\Delta t}{\Delta r} \left(\bar{q}_{r,i+\frac{1}{2},j}^n \frac{W_{i+1,j}^n - W_{i,j}^n}{\Delta r} - \bar{q}_{r,i-\frac{1}{2},j}^n \frac{W_{i,j}^n - W_{i-1,j}^n}{\Delta r} \right) + \frac{\Delta t}{\Delta z} \left(\bar{q}_{z,i,j+\frac{1}{2}}^n \frac{W_{i,j+1}^n - W_{i,j}^n}{\Delta z} - \bar{q}_{z,i,j-\frac{1}{2}}^n \frac{W_{i,j}^n - W_{i,j-1}^n}{\Delta z} \right) + \frac{\Delta t}{r_i} \bar{q}_{r,i,j}^n \frac{W_{i+1,j}^n - W_{i-1,j}^n}{2\Delta r},$$

and

$$\bar{q}_{r,i+\frac{1}{2},j}^n = (\bar{q}_{r,i+1,j}^n + \bar{q}_{r,i+1/2,j}^n)/2,$$

$$\bar{q}_{z,i,j+\frac{1}{2}}^n = (\bar{q}_{z,i,j+1}^n + \bar{q}_{z,i,j+1/2}^n)/2,$$

$$\bar{q}_{r,i,j}^n = Q \Delta r^2 \frac{|v_{r,i+1,j}^n - v_{r,i-1,j}^n|}{2\Delta r},$$

$$\bar{q}_{z,i,j}^n = Q \Delta z^2 \frac{|v_{z,i,j+1}^n - v_{z,i,j-1}^n|}{2\Delta z},$$

where Q is the artificial viscosity coefficient of order unity.

The code is based on the one originally developed and tested by Shibata and Uchida (1986). We developed the original code suitable to our present situation.

2.2.3 Lorentz-Force Term in the Equation of Motion

In this simulation, we calculate the Lorentz force $\mathbf{j} \times \mathbf{B}$ in the equation of motion as $(\mathbf{j} - \mathbf{j}_0) \times \mathbf{B}$ for the numerical stability, where \mathbf{j}_0 is the initial current density. This treatment is justified because we assume a current-free magnetic field ($\mathbf{j}_0 \equiv 0$) initially.

In this case the Lorentz-force term is expressed in a non-conservation form like $P(W) \partial U(W) / \partial r$ or $Q(W) \partial V(W) / \partial z$. We estimate discretized values of $P(W)$ or

$Q(W)$ as we estimate those of the source term $S(W)$ in the case of conservation form. We examined the effect of this modification by testing previous 2 or 2.5-dimensional MHD problems, for example, Low (1984) for checking the propagation of MHD discontinuity, Ugai and Tsuda (1979) for checking the magnetic reconnection, and Shibata and Uchida (1986) for checking the propagation of torsional Alfvén waves, etc., and could get almost the same results if strong shocks do not exist. (Even if strong shocks exist, the error was estimated to be less than 10%.) Since we treat the case in which strong shocks do not exist, we consider that we can obtain accurate enough results quantitatively by using our code.

2.3 Dimensionless Equation System

Let us now make the equation system (1)~(5) in the dimensionless form. First, we introduce three characteristic quantities, typical length r_0 , typical density ρ_0 and typical velocity v_0 . We normalize all variables by using these three quantities and their combinations and get the following dimensionless variables (primed variables). (We define typical time scale t_0 as r_0/v_0 .)

$$\begin{aligned} r' &= r/r_0, & \rho' &= \rho/\rho_0, & \mathbf{v}' &= \mathbf{v}/v_0, \\ t' &= t/(r_0/v_0), \\ p' &= p/(\rho_0 v_0^2), & \mathbf{B}' &= \mathbf{B}/(\rho_0 v_0^2)^{1/2}, & g' &= g/(v_0^2/r_0), & \eta' &= \eta/(r_0 v_0). \end{aligned} \quad (19)$$

Using these dimensionless quantities, we obtain the following dimensionless equation

system which take the same form as the dimensional equation system (1)~(5).

$$\frac{\partial \rho'}{\partial t'} + \nabla' \cdot (\rho' \mathbf{v}') = 0 \quad (20)$$

$$\rho' \left[\frac{\partial \mathbf{v}'}{\partial t'} + (\mathbf{v}' \cdot \nabla') \mathbf{v}' \right] + \nabla' p' - \mathbf{j}' \times \mathbf{B}' - \rho' g' = 0 \quad (21)$$

$$\frac{\partial \mathbf{B}'}{\partial t'} + \nabla' \times (-\mathbf{v}' \times \mathbf{B}' + \eta' \mathbf{j}') = 0 \quad (22)$$

$$\left[\frac{\partial}{\partial t'} + (\mathbf{v}' \cdot \nabla') \right] (\rho' \rho'^{-\gamma}) = 0 \quad (23)$$

$$\mathbf{j}' = \frac{1}{4\pi} \nabla' \times \mathbf{B}' \quad (24)$$

2.4 Initial Conditions and Dimensionless Parameters

2.4.1 Initial Conditions

First we adopt basic assumptions for simplicity as follows. We take the z -axis along the rotational axis of the disk. We assume that the star is located at the origin and the magnetic dipole moment of the star is parallel to the z -axis. As discussed in the previous section 1.3, we treat in this paper the case in which the star is non-rotating, for the first step. We neglect the self-gravity of the disk itself.

Due to the practical limitations of the numerical simulations, we adopt the following simplifications for the initial conditions. (1) The star has a spherical isothermal hydrostatic corona. (We do not treat the interior of the star and take the surface as one of the boundaries of calculations (see the next section 2.5).)

(2) A dense cool disk is rotating around the star in approximately a rotational equilibrium. (For simplicity we do not give the detailed structure for the initial

disk and let the disk approach the equilibrium configuration with all forces acting on it, namely, let it relax into the equilibrium by giving the initial geometry and density assumed to be almost uniform throughout the disk.) (3) The magnetic field is assumed to be initially dipolar for the stellar field, and uniform and parallel to z-axis for the disk field. (The latter is probably an over-simplification, because the contracted disk material from the interstellar cloud should have produced an hourglass shape magnetic field configuration already at this phase, but we use this simplified assumption since the very essential effect can be reproducible.) There appears a magnetically neutral ring in the equatorial plane. The inner edge of the disk is assumed to be outside the location of the neutral ring.

The initial conditions are summarized in the vector form,

$$\rho = \rho_{\text{corona}} + \rho_{\text{disk}}, \quad (25)$$

$$p = p_{\text{corona}}, \quad (26)$$

$$(-\nabla p_{\text{corona}} + \rho_{\text{corona}} \mathbf{g} = 0, \quad \mathbf{g} = -\nabla \psi_{\text{point mass}}) \quad (27)$$

$$\mathbf{B} = \mathbf{B}_{\text{dipole}} + \mathbf{B}_{\text{uniform}}, \quad (28)$$

$$\mathbf{v} = \mathbf{v}_{\text{disk}}. \quad (29)$$

(See Figure 2.4.)

2.4.2 Dimensionless Parameters

We put the reference point $(r_0, 0)$ inside the disk, introducing the typical length r_0 , and take the coronal density and the coronal sound velocity at the reference point as the typical density ρ_0 and the typical velocity v_0 , respectively (see equation (19)).

Then the initial conditions we are considering may be expressed in a dimensionless scalar form :

$$\rho' = \exp \left[\frac{\gamma}{\epsilon} \left(\frac{1}{r'} - 1 \right) \right] + q f_d(r', z'), \quad (30)$$

$$p' = \frac{1}{\gamma} \exp \left[\frac{\gamma}{\epsilon} \left(\frac{1}{r'} - 1 \right) \right], \quad (31)$$

$$v'_r = 0, \quad (32)$$

$$v'_\phi = \alpha \sqrt{\frac{1}{\epsilon r'}} f_d(r', z'), \quad (33)$$

$$v'_z = 0, \quad (34)$$

$$B'_r = \sqrt{\frac{\gamma \beta}{8\pi}} \left(\frac{1}{r_n^3} - 1 \right)^{-1} \frac{3r'z'}{(r'^2 + z'^2)^{\frac{3}{2}}}, \quad (35)$$

$$B'_\phi = 0, \quad (36)$$

$$B'_z = \sqrt{\frac{\gamma \beta}{8\pi}} \left(\frac{1}{r_n^3} - 1 \right)^{-1} \left[\frac{2z'^2 - r'^2}{(r'^2 + z'^2)^{\frac{3}{2}}} + \frac{1}{r_n^3} \right], \quad (37)$$

$$\psi' = -\frac{1}{\epsilon \sqrt{(r'^2 + z'^2)}}, \quad (38)$$

$$f_d(r', z') = \frac{1}{4} \left[1 + \tanh\left(\frac{r' - r'_d}{\Delta_d}\right) \right] \left[1 - \tanh\left(\frac{z' - z'_d}{\Delta_d}\right) \right], \quad (39)$$

with dimensionless parameters defined as follows,

$$\begin{aligned} \epsilon &\equiv \gamma \frac{p_0}{GM_* \rho_0 / r_0}, \\ \beta &\equiv \frac{p_0}{B_0^2 / 8\pi}, \quad r'_n \equiv \left(\frac{B_*}{2B_u} \right)^{\frac{1}{2}}, \quad \left(B_0 = B_u - B_* \left(\frac{R_*}{r_0} \right)^3 \right) \\ \alpha &\equiv \frac{v_{\phi 0}}{(GM_* / r_0)^{\frac{1}{2}}}, \quad q \equiv \frac{\rho_d}{\rho_0}, \quad r'_d \equiv \frac{r_d}{r_0}, \quad z'_d \equiv \frac{z_d}{r_0}, \end{aligned} \quad (40)$$

where M_* is the stellar mass, R_* is the stellar radius, B_* is the stellar field strength at the pole, ρ_d is the density of the disk, r_d is the inner radius of the disk, z_d is the thickness of the disk, B_u is the strength of the uniform field, and B_0 , p_0 and $v_{\phi 0}$ are the strength of the magnetic field, the coronal pressure and the rotational velocity

of the disk, at the inner edge of the disk, respectively.

ϵ , β and α represent the ratio of the coronal thermal energy to the gravitational energy, the ratio of the coronal gas pressure to the magnetic pressure and the ratio of the rotational velocity of the disk to the local Keplerian velocity, respectively, all at the reference point $(r_0, 0)$. q is the ratio of the disk density to the coronal density at the radius r_0 . r'_n is the normalized radius of the magnetically neutral ring and is related to the ratio of the strength of the dipolar field to that of the uniform field.

$f_d(r', z')$ is defined such that $f_d(r', z') = 1$ well inside the disk ($r' \geq r'_d$, $z' \leq z'_d$) and $f_d(r', z') = 0$ well outside the disk. (Δ_d is the normalized thickness of the transition region.)

2.5 Simulation Region and Boundary Conditions

The total simulation region in the r' - z' plane is taken to be $0 \leq r' \leq r'_{max}$ and $0 \leq z' \leq z'_{max}$, where $r'_{max} = 2.5$ and $z'_{max} = 5.0$. The numbers of the mesh points used in our calculations are $(N_r, N_z) = (355, 295)$. We assign the mesh points (320, 250) in the region of our main concern ($0 \leq r' \leq 1.0$ and $0 \leq z' \leq 1.0$) by introducing meshes which are variable in r' and z' . (Hereafter, in this section, we omit the prime '.)

2.5.1 Boundary Conditions at Outer Boundaries, r -axis and z -axis

We use free boundary conditions at the outer boundaries ($r = r_{max}$ and $z = z_{max}$), for example,

$$\rho(r_{max}, z, t) = \rho(r_{max}, z, 0) + \rho(r_{max} - \Delta r, z, t) - \rho(r_{max} - \Delta r, z, 0),$$

$$\begin{aligned} p(r_{max}, z, t) &= p(r_{max}, z, 0) + p(r_{max} - \Delta r, z, t) - p(r_{max} - \Delta r, z, 0), \\ v_r(r_{max}, z, t) &= v_r(r_{max}, z, 0) + v_r(r_{max} - \Delta r, z, t) - v_r(r_{max} - \Delta r, z, 0), \\ v_\phi(r_{max}, z, t) &= v_\phi(r_{max}, z, 0) + v_\phi(r_{max} - \Delta r, z, t) - v_\phi(r_{max} - \Delta r, z, 0), \\ v_z(r_{max}, z, t) &= v_z(r_{max}, z, 0) + v_z(r_{max} - \Delta r, z, t) - v_z(r_{max} - \Delta r, z, 0), \\ B_r(r_{max}, z, t) &= B_r(r_{max}, z, 0) + B_r(r_{max} - \Delta r, z, t) - B_r(r_{max} - \Delta r, z, 0), \\ B_\phi(r_{max}, z, t) &= B_\phi(r_{max}, z, 0) + B_\phi(r_{max} - \Delta r, z, t) - B_\phi(r_{max} - \Delta r, z, 0), \\ B_z(r_{max}, z, t) &= B_z(r_{max}, z, 0) + B_z(r_{max} - \Delta r, z, t) - B_z(r_{max} - \Delta r, z, 0), \end{aligned} \quad (41)$$

and symmetric boundary conditions at the equatorial plane ($z = 0$),

$$\begin{aligned} \rho(r, -\Delta z, t) &= \rho(r, \Delta z, t), \\ p(r, -\Delta z, t) &= p(r, \Delta z, t), \\ v_r(r, -\Delta z, t) &= v_r(r, \Delta z, t), \\ v_\phi(r, -\Delta z, t) &= v_\phi(r, \Delta z, t), \\ v_z(r, -\Delta z, t) &= -v_z(r, \Delta z, t), \\ B_r(r, -\Delta z, t) &= -B_r(r, \Delta z, t), \\ B_\phi(r, -\Delta z, t) &= -B_\phi(r, \Delta z, t), \\ B_z(r, -\Delta z, t) &= B_z(r, \Delta z, t), \\ v_z(r, 0, t) &= 0, \\ B_r(r, 0, t) &= 0, \\ B_\phi(r, 0, t) &= 0, \end{aligned} \quad (42)$$

and at the z -axis ($r = 0$),

$$\begin{aligned}
 \rho(0, z, t) &= \rho(0, z, 0) + \rho(\Delta r, z, t) - \rho(\Delta r, z, 0), \\
 p(0, z, t) &= p(0, z, 0) + p(\Delta r, z, t) - p(\Delta r, z, 0), \\
 v_r(0, z, t) &= 0, \\
 v_\phi(0, z, t) &= 0, \\
 v_z(0, z, t) &= v_z(\Delta r, z, t), \\
 B_r(0, z, t) &= 0, \\
 B_\phi(0, z, t) &= 0, \\
 B_z(0, z, t) &= B_z(0, z, 0) + B_z(\Delta r, z, t) - B_z(\Delta r, z, 0).
 \end{aligned} \tag{43}$$

2.5.2 Boundary Condition at the Stellar Surface

We set the inner boundary for the numerical simulation at the stellar surface, because we are not concerned with the detailed inner structure of the central star in this simulation. It is, however, difficult to solve precisely the initial-boundary value problem at the stellar surface with the limited numbers of mesh points. So we introduce a thin shell-like damping region outside the stellar surface where the disturbance in all the physical quantities except for the magnetic field are damped as follows.

$$\begin{aligned}
 \rho(r, z, t) &= \rho(r, z, t) - h_d(r, z)[\rho(r, z, t) - \rho(r, z, 0)], \\
 p(r, z, t) &= p(r, z, t) - h_p(r, z)[p(r, z, t) - p(r, z, 0)], \\
 v_r(r, z, t) &= v_r(r, z, t) - h_v(r, z)[v_r(r, z, t) - v_r(r, z, 0)],
 \end{aligned} \tag{44}$$

$$\begin{aligned}
 v_\phi(r, z, t) &= v_\phi(r, z, t) - h_v(r, z)[v_\phi(r, z, t) - v_\phi(r, z, 0)], \\
 v_z(r, z, t) &= v_z(r, z, t) - h_v(r, z)[v_z(r, z, t) - v_z(r, z, 0)].
 \end{aligned}$$

Damping factors $h_d(r, z)$, $h_p(r, z)$, $h_v(r, z)$ are determined so that they are equal to zero outside the damping region and unity well inside the damping region. Then in actual calculations, we are free from the problems concerning the inner numerical boundary, because disturbances, being damped (first in the inner high density part of the corona and) finally in the damping region, will not reach the inner numerical boundary at the stellar surface where realistic assignment of physical boundary conditions requires too much for the numerical simulation.

This damping region may be regarded as a "physical boundary". To damp the disturbances in the density, the pressure and the velocity field means the effective sink of mass (the fallen mass is readily absorbed in the high density surface part of the star), the effective cooling (the liberated heat is emitted away), and the effective friction (due to the high-density stellar gas), respectively. Since the disturbance in the magnetic field is not damped, the frozen-in condition holds and the identification of the lines of force is maintained.

Let us consider the transfer of the angular momentum of the accreting material to the star via the Alfvén wave, or the magnetic stress. As the inertia of the star is much larger than that of the accreting mass, the stellar surface will behave as a fixed boundary in the corotation frame of the star. If the Alfvén wave with the angular momentum density l propagates to the star, it is perfectly reflected and the Alfvén wave with the angular momentum $-l$ is transmitted outward. In this case, the angular momentum $2l$ is transferred to the inside of the star. In our simulation, we can represent such reflections of Alfvén waves at the stellar surface, because the

Alfvén wave propagating into the damping region is finally reflected almost perfectly. (Note that a damping boundary with the damping factor unity behaves as a fixed boundary.) We performed 1.5-dimensional MHD simulation and tested the reflection of Alfvén waves in the damping region which is defined as equation (44) and found that the reflectivity is above 95%.

In this simulation in which the damping region is set outside the stellar surface, we cannot deal with such phenomena as the accreting mass crashing onto the surface to produce a hot X-ray emitting region or the production of the recoiled shocks dealt with by Uchida and Shibata (1984). We here mainly deal with the processes due to the interaction between the magnetized disk with the magnetosphere at the interface.

2.6 Resistivity Model

Magnetic reconnection occurs through the magnetic diffusion around the neutral point, but its detailed mechanism, especially the origin of the anomalous resistivity, is not clear yet. (In the steady magnetic reconnection, the magnetic flux convected into the diffusion region around the neutral point must diffuse out. This requires the "anomalous" resistivity whose value is much larger than the classical resistivity due to the Coulomb collision.) One idea for the anomalous resistivity is that it is due to the excitation of plasma turbulence generated in the interaction between waves and particles' motions. There are some candidates for the microscopic instabilities which disturb particles' motions and lead to the anomalous resistivity. Lower Hybrid Drift Instability (LHDI) is claimed to be the most likely one, which is excited by the diamagnetic current in rather weak magnetic field where electrons are magnetized

and ions are not (Huba et al. 1978, Hoshino 1991).

Sato and Hayashi (1979) considered that the magnetic reconnection is induced by setting up the anomalous resistivity due to the enhanced diamagnetic current around the neutral point. Following them, we assume the anomalous resistivity model as follows:

$$\eta'(r', z') = \eta'_0 f_n(r', z'), \quad (45)$$

where

$$\eta'_0 \cong \begin{cases} \eta'_{max}, & \text{if } j_{\phi n}' > j_c'; \\ 0, & \text{otherwise.} \end{cases}$$

and $f_n(r', z')$ is the factor which localizes the finite resistivity only around the magnetically neutral point. Then the normalized resistivity of order η'_{max} is induced around the neutral point if the current at the neutral point $j_{\phi n}'$ exceeds the critical value j_c' . We take the typical value of the enhanced current in the case of no resistivity as j_c' .

If we define the magnetic Reynolds number R_m as $1/\eta' = v_0 v_0 / \eta$ (see equation (19)), the "anomalous" magnetic Reynolds number R_{mmin} around the neutral point corresponding to the anomalous resistivity η'_{max} is order of $1/\eta'_{max}$. Typically we adopt the "anomalous" magnetic Reynolds number R_{mmin} of order of 10. (Due to the finite numerical diffusion, the background magnetic Reynolds number is $\sim 10^3$ in the above definition.)

Chapter 3

Numerical Results

3.1 Physical Parameters and Outline of the Results

In this chapter, we will mainly discuss the result of the typical case, where we choose numerical parameters introduced in section 2.4 as follows; $\epsilon = 1.2$, $\beta = 1.3$, $r'_n = 0.63$, $R'_c = 0.10$, $\alpha = 0.8$, $q = 60.0$, $r'_d = 0.79$, $z'_d = 0.08$. These parameters correspond to the following physical values;

The normalizing length, density, velocity and time-scale are, respectively,

$$r_0 \sim 10^{12.5} \text{cm}, \rho_0 \sim 10^{-12.5} \text{gcm}^{-3}, v_0 \sim 10^{6.5} \text{cms}^{-1} \text{ and } t_0 \sim 10^{6.0} \text{s}.$$

The radius, mass of the central star and the dipolar field strength at the pole are, respectively,

$$R_* \sim 10^{11.5} \text{cm}, M_* \sim 10^{32.5} \text{g} \text{ and } B_* \sim 10^{3.5} \text{G}.$$

The density, surface density, temperature of the disk and the uniform field strength are, respectively,

$$\rho_d \sim 10^{-9.5} \text{gcm}^{-3}, \Sigma \equiv \rho_d z_d \sim 10^2 \text{gcm}^{-2}, T_d \sim 10^9 \text{K} \text{ and } B_0 \sim 10^4 \text{G}.$$

We discuss the numerical results in the following with non-dimensional values with the prime ' omitted. The correspondence to the values in the actual case will be discussed in the next chapter.

Before we discuss the details, we give the outline of the results of simulations. Figures 3.1(a)~(t) show time evolutions of various physical quantities in the poloidal plane. The disk continues to contract due to the magnetic braking by the large-scale magnetic field penetrating itself. The accreting disk compresses the region around the neutral ring at the interface between the disk and the magnetosphere of the central star. This compression causes the enhancement of the diamagnetic current which produces the anomalous resistivity. Then the magnetic reconnection between the large-scale field of the disk and the magnetospheric field is induced and at the same time the disk material is transferred to the magnetosphere. (Here we define the magnetosphere of the central star as the region where the magnetic field of the central star dominates the plasma motion.) Since we assume in this first approach that the central star is not rotating for simplicity, the disk material transferred to the magnetosphere is magnetically braked by the central star via the magnetospheric field and most of it falls to the stellar polar crown along the magnetospheric field. On the other hand, the low density part near the surface of the disk and the coronal material frozen to the reconnected field line are ejected toward bipolar directions and form a cylindrical collimated jet. This jet is mainly accelerated by the $\mathbf{j} \times \mathbf{B}$ force associated with the magnetic reconnection, although the ultimate source of energy of the jet in the present case is the gravitational potential energy of the accretion disk material, once stored in the magnetic stress.

3.2 Disk Accretion by Magnetic Braking

Since the corona is initially static*, the velocity shear between the disk and the corona creates the toroidal magnetic field, and transmit the torsional Alfvén wave both to the corona and the disk (Figure 3.3(a)(b)(c); $t=0.5$). That is, the angular momentum of the disk is transferred to the corona through the magnetic stress (Figure 3.1(i)(j)). This magnetic braking continuously acts on the disk and the disk material can contract by losing its angular momentum. Figure 3.2 shows the time evolution of the distribution of the specific angular momentum along a poloidal flux tube penetrating the disk in the early stage ($0.0 \leq t \leq 1.0$). We can see that the coronal material quickly gets the angular momentum as the torsional Alfvén wave passes through that part, while the material of the disk part continues to lose the angular momentum, especially near the surface.

Note that in the so-called "standard accretion model" ever discussed widely (for example, Shakura and Sunyaev 1973), the angular momentum of the disk is assumed to be transferred readily in the disk plane to the part of the disk at a larger radius through the viscous stress associated with the angular velocity shear, and the half of the gravitational energy is liberated as the thermal energy through the viscous heating, while in our case the angular momentum of the disk is transferred vertically to the corona from the disk surface through the magnetic stress, and the excess of the gravitational energy is carried away as the Poynting flux.

Uchida and Shibata (1985) and Shibata and Uchida (1986) showed the formation of the bipolar outflow from the surface of the disk which is penetrated by

* This is an assumption for simplicity. Even if the corona near the disk is initially rotating with the disk, the gradient (shear) in the rotational velocity toward infinity will be established, and what follows is qualitatively similar.

a large-scale magnetic field brought into it in the contraction process from the interstellar gas. This outflow is initially accelerated by the gradient of the toroidal magnetic field generated by the disk rotation and then accelerated together with the magneto-centrifugal effect. When this type of outflow is formed, the efficiency of the angular momentum loss becomes larger because the outflow material also carries away the angular momentum. (A part of the gravitational energy is also converted to the kinetic energy of the outflow.) In our present parameter range, this type of outflow from the surface of the disk is not efficiently formed (figure 3.1(c)) and the main carrier of the angular momentum is the magnetic stress. This is because the inertia of the rotating disk is not so large as to generate the gradient of the toroidal magnetic field large enough to form that type of outflow. (We will discuss the case in which the density of the disk is large and thus the untwisting jet is formed, in section 3.6.)

3.3 Driven Reconnection by Disk Accretion

The disk material losing its angular momentum by the magnetic braking spirals in toward the central star and the large-scale magnetic field penetrating the disk material is pushed to the magnetospheric field of the opposite polarity at the interface. This compression enhances the toroidal current j_ϕ around the neutral point which holds the opposite poloidal magnetic fields. From our resistivity model as discussed in section 2.6, the enhanced current leads to the production of the anomalous resistivity. (We can recognize the current layer of modified X-type configuration in Figure 3.1(n).) Then the magnetic diffusion around the neutral point induces the

magnetic reconnection between the large-scale field of the disk and the magnetospheric field (Figure 3.1(d)). We can say that this is the reconnection "driven by the disk accretion".

The magnetic reconnection occurs not within the poloidal plane, but in three dimensions by 2.5-dimensional configuration. Figures 3.3(a)~(c) are the perspective view of the lines of force labeled with the same value of the flux function rA_ϕ . (In the axial symmetry case, a line of force is identified with the value of the flux function and a line of force of the disk with some value of the flux function reconnects the line of force of the magnetosphere having the same value of the flux function.) Initially the magnetosphere consisting of the closed lines of force is surrounded by the hourglass-type lines of force penetrating the disk. By the time just before the reconnection, $t \sim 1.5$, both the magnetic fields penetrating the disk and the magnetosphere are squeezed and distorted by the disk accretion. The topology of the magnetic fields changes through the reconnection, that is, the closed lines of force are opened up, and the lines of force penetrating the disk are then changed to the stellar polar-open fields. After the reconnection $t = 2.0 \sim 3.5$, the distortion of the lines of force relaxes and the field lines are synchronized with the stellar rotation as the torsional Alfvén waves propagate outward. Since we assume the non-rotating star, the field lines finally come to be static in space.

Figure 3.4(a),(b) show the time variation of the flux function rA_ϕ , and the radius of the neutral ring r_0 . The value of the flux function at the neutral point is related to the amount of the closed flux of the central star. In the earlier phase ($t \leq 1.5$) the radius of the neutral ring r_0 quickly decreases although the flux function rA_ϕ has an almost constant value, because the initial magnetic field is weak, and hence, less magnetic flux is distributed near the neutral ring. In the later phase ($t \geq 1.5$)

the flux function increases almost constantly, which means that the reconnection proceeds at an almost constant rate. On the other hand, the radius of the neutral ring which coincides with the inner edge of the disk has an almost constant value. This value is determined by the interaction of the magnetosphere with the disk accretion rather than with the large-scale magnetic field, because the large-scale magnetic field is passive to the motion of the disk material. Figure 3.5(a) shows the distribution of the various forces in the equatorial plane near the neutral point. (The neutral point is at $r_0 \sim 0.25$. The diffusion region extends $0.24 \leq r \leq 0.26$.) We can see that at the inner edge of the disk ($r_0 \sim 0.24$) the Lorentz force (= the magnetic pressure gradient of the magnetosphere) balances the gas pressure gradient. This high pressure around the neutral point is mainly due to the compression by the disk accretion and partly due to the Joule heating. That is, the magnetic pressure of the magnetosphere balances the accretion pressure through the gas pressure around the neutral point (Figure 3.5(b)).

3.4 Mass and Angular Momentum Transfer through Magnetic Reconnection

We consider the transfer of the mass and the angular momentum within a flux tube initially penetrating the disk. The mass and the angular momentum are initially concentrated within the disk part. Before the interaction with the magnetosphere of the central star, the disk part interact with the coronal part, and the excess angular momentum for accretion is transferred to the coronal gas through the magnetic stress, but the mass of the disk is not transferred.

After the reconnection with the magnetospheric field, the flux tube is then rooted to the stellar surface, which means that the disk material with its angular momentum is transferred to the magnetosphere.* Finally most of the disk material accretes to the stellar surface by losing the angular momentum through the interaction with the magnetospheric field of the non-rotating star. Figure 3.7(a) shows the motion of a fluid particle which is initially located in the disk and finally accretes onto the central star, together with the field line which the fluid particle is frozen-in. Figure 3.7(c) shows the time variation of the specific angular momentum of the fluid particle. At the time $t = 3.0$, the magnetic reconnection occurs and the particle is transferred to the magnetospheric field. Through the magnetic action (the reflection of torsional Alfvén waves at the stellar surface), the particle oscillates in the azimuthal direction and gradually loses its angular momentum, and finally it is synchronized with the stellar rotation. In this case, since the star is at rest, the rotational motion of the particle is stopped (that is, magnetically braked by the

* In fact, the mass transfer and the magnetic reconnection do not occur simultaneously. The anomalous resistivity around the neutral point forms the magnetic diffusion region of a finite size. (Here we define the diffusion region as the region where the diffusion term is larger than the convection term in the induction equation, that is, where the materials effectively decouple from the magnetic field.) Since the magnetic reconnection in our case is highly asymmetric (the one-sided inflow in contrast to the usual X-type reconnection), and is affected by the gravitational field one-sided toward the star, the decoupled materials in the diffusion region move inwards by the effect of the gravity. When they escape from the diffusion region, a part of them recouple with the open, reconnected field lines, but the other part recouple with the closed field lines which will reconnect later.

star), and then falls toward the star by the gravity ($t = 3.3 \sim$) (see Figure 3.7(b)). (The case of a rotating star will be discussed in section 4.1.) On the other hand, the material in the layer near the surface of the disk is ejected together with the coronal gas along the reconnected field lines with open ends, and forms a collimated bipolar jet (see section 3.4). Thus the disk material splits into the accreting material and the jet material, that is, the inflow and the outflow coexist with in a open, reconnected flux tube.

We estimate \dot{M}_{jet} (the mass loss rate in the form of the jet), and \dot{M}_{acc} (the mass accretion rate in the disk) as follows.

$$\begin{aligned} \dot{M}_{jet} &= 2 \int_{J_{et}} dr 2\pi r \rho(r, z_0) v_z(r, z_0) \quad (z_0 \sim 0.5), \\ \dot{M}_{acc} &= -2 \int_{disk} dz 2\pi r_0 \rho(r_0, z) v_r(r_0, z) \quad (r_0 \sim 0.3). \end{aligned}$$

We get $f \equiv \dot{M}_{jet}/\dot{M}_{acc} \sim 0.1$ in the stage when the jet is formed continuously ($t \geq 3.0$).

The excess angular momentum of the disk material to accrete on the stellar surface from the reconnecting point (= the inner edge of the disk) is loaded on the open reconnected field line and finally redistributed to both the star and the corona (or the jet) through magnetic action. This process may be explained semi-quantitatively as follows: First of all, due to the loading of the excess specific angular momentum $l_i (> 0)$ on the reconnected line of force, the inward Alfvén wave with the angular momentum $l_{in} (> 0)$ and the outward Alfvén wave with $l_{out} (> 0)$ are transmitted from the reconnecting point ($l_{in} + l_{out} = l_i$). Since the stellar surface behaves as a rigid boundary, the inward Alfvén wave is reflected at the stellar surface and the outward Alfvén wave with the angular momentum $-l_{in} (< 0)$ is transmitted. (Through this reflection the star receives the angular momentum $l_{star} = 2l_{in}$, but here we do not consider the effect of this on the stellar rotation, since the star has

an angular momentum much larger than l_{in} .) The outer corona receives the angular momentum l_{out} first and then $-l_{in}$, so finally receives $l_{corona} = l_{out} - l_{in}$ (where, $l_{star} + l_{corona} = l_{in} + l_{out} = l_1$).

We can confirm the above discussion roughly in the results of the simulation. Figure 3.6(a) shows the propagation of torsional Alfvén waves carrying the angular momentum along a field line rooted to the star during the interaction. (At $t = 1 \sim 2$ the closed line of force which has not yet reconnected with the large-scale magnetic field is distorted. This is because of the effect of the finite size of the diffusion region as discussed above, that is, the disk material with angular momentum is transferred to the closed line of force through the magnetic diffusion before the reconnection occurs.) Figure 3.6(b),(c) show the angular momentum distribution and the angular momentum flux distribution along this line of force. (If the positive angular momentum is transferred inward, the sign of the angular momentum flux is plus.) From Figure 3.6(c) we can see that in the earlier stage ($t = 1 \sim 3$) the positive angular momentum is transferred both inward and outward from the reconnecting point. In the later stage ($t = 4 \sim 9$) the negative angular momentum is transferred outward, which almost cancels the positive angular momentum transferred outward first. In Figure 3.6(c) if we take the value at $s_p \sim 0.1$, only the positive torque is acting on the stellar surface during the interaction (= the reflection of the torsional Alfvén wave) and thus the star receives most of the positive angular momentum which the disk material had at the reconnecting point. On the other hand, on the outer surface ($s_p \sim 0.4$) the positive torque acts in the early phase ($t = 3 \sim 4$), and then the negative torque acts in the later phase ($t = 5 \sim 9$) and almost cancel the previous positive torque. We note that in the inner region ($s_p \leq 0.2$) the magnetic field is so strong that the angular momentum is transferred mainly through the

magnetic stress, while in the outer region ($s_p \geq 0.6$) the angular momentum is transferred through both the magnetic stress and the material kinetic stress, which may be due to the interaction of the torsional Alfvén wave with the jet material (Figure 3.6(d); see next section).

3.5 Acceleration of Collimated Jet Associated with MHD wave Propagation

In this section we examine the acceleration mechanism of the jet. Figure 3.8(d) shows the time variation of the absolute value of the velocity of a test fluid particle ejected in the jet from the surface layer of the disk. We can see that the acceleration occurs two times at $t \sim 2.8$ and $t \sim 3.0$ and that the fluid particle finally gets a escape velocity. Both accelerations at $t \sim 2.8$ and $t \sim 3.0$ are due to the Lorentz force (Figure 3.8(b)). We decompose the Lorentz force ($j \times B$) into three terms, $j_p \times B_t$, $j_t \times B_p$ and $j_p \times B_p$, and examine the works done by each of them. Figure 3.8(c) shows that the first acceleration at $t \sim 2.8$ is mainly due to the $j_t \times B_p$ and the second acceleration at $t \sim 3.0$ is mainly due to the $j_p \times B_p$. This means that the first acceleration occurs in the poloidal plane due to the distortion of the poloidal field and the second one occurs in the toroidal direction by the magnetic tension.

These accelerations by the Lorentz force are associated with the MHD waves which propagate along the reconnected field lines in three dimensions so as to relax the distortion of the reconnected field lines, and so as to synchronize the reconnected field lines with the stellar rotation. (The latter inclination is due to the fact that the accreting mass is much smaller than the stellar mass and that the stellar surface

behaves as a fixed boundary for the reflection of the torsional Alfvén waves, as discussed in section 3.4.) The distortion of the field lines in the poloidal plane is due to the topology change by the magnetic reconnection, while the distortion in the toroidal direction is not only due to the topology change but also due to the rotational velocity shear between the magnetosphere and the disk at the reconnecting point.

MHD waves which carry the information of the reconnection are transmitted both inwards and outwards from the reconnecting point along the stellar open (reconnected) field line. The inward Alfvén wave is reflected at the stellar surface which behaves as a rigid boundary, and then the outward Alfvén wave which carries the information of the stellar rotation is transmitted. We can recognize these wave fronts as current layers in the current distribution in the poloidal plane (Figure 3.1(n): j_ϕ , (p): j_z). Among these MHD waves, two outgoing waves involve in the jet acceleration. The fluid particle which forms the jet passes through the two wave fronts and is accelerated at each time.

The first outgoing wave propagates in the poloidal plane as an MHD-slow mode wave. This wave corresponds to the MHD-slow shock in the Petek's reconnection model (1964), although in this case the wave does not evolve to a shock. (This is due to the field configuration described below and the low plasma β (~ 5) around the reconnecting point.) Figure 3.9(a),(b) shows the distribution of the toroidal current j_ϕ , and the velocity field around the neutral point in the poloidal plane. The first acceleration by $j_z \times B_\phi$ in the poloidal plane occurs at the current layer which corresponds to the MHD-slow mode wave front. We can see that the inward velocities in the surface layer of the disk and in the corona are changed to the upward velocities at the current layer extended from the neutral point. The

strength of the poloidal magnetic field is weakened across this toroidal current layer in the direction of the flow (MHD-slow mode), although it is not so clear in the Figure 3.1(d) because the kink of the field line is small and the angle between the current layer and the poloidal magnetic field is small. The figure 3.8(a) shows the motion of a test fluid particle ejected in the jet, together with the field line which the fluid particle frozen-in. From the side view, we can see the particle motion in the poloidal plane and that the particle is accelerated by the kink of the field line like a "slingshot".

Next we consider the second acceleration by $j_r \times B_\phi$ in the toroidal direction, which is associated with the propagation of the outgoing torsional Alfvén wave reflected at the stellar surface. The top view in Figure 3.8(a) shows the motion of the fluid particle in the toroidal direction. The reflected torsional Alfvén wave synchronize the motion of the line of force with the stellar rotation and thus carries the reverse angular momentum in terms of the rotational direction of the disk. Thus as the particle in forward rotation passes through the torsional Alfvén wave, it is first braked and then is accelerated in the reverse direction like "flapping" and gets the poloidal momentum magneto-centrifugally. It finally stops the reverse rotating, that is, synchronized with the stellar rotation. We can see in Figure 3.1(i) that the part of the jet (which is just after the second acceleration) is in the reverse rotation, and the other part of the jet is almost at rest. The amplitude of the wave becomes large as the wave propagates into the outer low-density region. We examine the time variation of the physical properties of a test fluid particle which is first located in the outer corona and passes through the outgoing torsional Alfvén wave (Figure 3.10(a)(b)(c)). During the strong magnetic braking at the wave front, the fluid particle is compressed, the temperature and the entropy of the particle rise, and the

toroidal field is weakened. Thus the front part of this torsional Alfvén wave can be recognized as an MHD-slow mode shock although it is broadened, and thus not so strong. Note that this MHD-slow mode is due to the balancing the gas pressure and the "toroidal" magnetic pressure, in contrast to the MHD-slow mode associated with the $j_i \times B_p$ acceleration, where the gas pressure balances with the poloidal magnetic pressure.

In Figure 3.1(f), we can see that the pressure in the jet region is high compared with the ambient medium, which is due to the MHD-slow mode compression or slow mode shock discussed above. (Figure 3.1(t) show that the total pressure is continuous across the wave front. Namely the gas pressure balances the magnetic pressure, which means that the waves are MHD slow mode.) It is not so clear whether the jet is heated or not by this compressional wave or shock, because of the initial non-uniform temperature distribution (the initial temperature of the disk material was low). But in the part of the jet region, which consists of the coronal material, the temperature is apparently higher than the initial isothermal temperature (Figure 3.1(h)). This may be due to the shock heating discussed above, because the entropy is also high compared to the ambient medium (Figure 3.1(q)). The Joule heating around the neutral point which is another heating source does not contribute to heating the jet, because all the disk material which enter the diffusion region and suffer the Joule heating fall toward the star, not forming the jet.

3.6 The Case of High-Density Disk

Here, we show the results of the case in which the initial density of the disk is larger

($q=120$). In this case the ratio of the magnetic energy to the gas energy is small compared with the typical case, and thus the magnetic fields are passive to the disk motion.

Figure 3.11 shows the time evolution of the velocity field(a), the field lines(b), the toroidal current(c), the test particles(d), the toroidal magnetic field(e) and the toroidal velocity(f) in the poloidal plane for the case of larger q ($q=120$) in the later stage ($t = 2.6 \sim 3.1$). The development of the system is roughly the same as the typical case, but we can see two effects coming from the relatively weak magnetic field.

The first one is the formation of the untwisting jet from the surface of the disk penetrated by the large-scale field (Uchida and Shibata 1985, Shibata and Uchida 1986). This is because the inertia of the disk rotation is large compared with the typical case and then the accumulation of the toroidal field near the disk surface is strong, which leads to formation of the untwisting jet. From the figure of the poloidal velocity field (Figure 3.11(c)), we cannot clearly distinguish this jet from the jet associated with the magnetic reconnection at the interface between the disk and the magnetosphere. But we can recognize that the inner part of the flow has a reverse toroidal velocity, which indicates the jet associated with the magnetic reconnection, and that the outer part has the same rotational direction as the disk, which indicates the untwisting jet (Figure 3.11(f)). Thus we demonstrated that the two types of jets in different origins can be formed in the vicinity of the central star (See section 4.2). One is the jet coming from the interface between the disk and the magnetosphere and is associated with the magnetic reconnection. The other is the untwisting jet coming from the surface of the inner part of the disk penetrated by the large-scale magnetic field.

Another interesting point is the formation of magnetic islands associated with the secondary magnetic reconnection. Because of the high density of the disk material, or the relatively weak magnetic fields, the reconnected lines cannot lift up the loaded disk material (the "slingshot" does not occur readily) (Figure 3.11(b); $t \sim 2.6$), which lead to the secondary magnetic reconnections, and multiple magnetic islands are formed ($t \sim 2.8$). We can recognize the formation of magnetic islands also from the figures of j_ϕ (c) and test particles (d). Note that magnetic islands (Figure 3.12) have "helical" structures in three dimensions, because the secondary reconnections occur between the opposite poloidal field lines having toroidal components. Since the secondary reconnections cut off the heavy part of the disk material, the field lines can carry up and accelerate the rest part of the disk material ($t = 2.8 \sim 3.1$). Note that magnetic islands which are cut off from the field lines rooted to the stellar surface keeps its rotational direction which is the same as the disk, while the other part of the disk material frozen to the stellar open field lines have opposite rotational velocity discussed in section 3.5 (Figure 3.11(f)). The heavy part of the disk material confined within the magnetic island once again reconnects with the open field of the star (the tertiary magnetic reconnection) (Figure 3.11(b); $t = 3.0$) and then accretes to the polar crown.

Chapter 4

Discussion

4.1 The Effect of the Stellar Rotation

In the present study we, as a first step, concentrated ourselves on the case in which the stellar rotation was not considered. In actual astrophysical cases, however, the stellar rotation is necessary to take into account. In this section we first discuss what kind of effects the rotation of the star would introduce. We here consider the coupling effect between the stellar rotation and the jet formation, which introduces the magneto-centrifugal acceleration of the jet, and thus the magnetic braking of the star by the production of the jet along the open field lines.

In the case in which the star is rotating, the corotation radius r_c where the angular velocity of the disk coincides with that of the star is an important factor. (The corotation radius was infinity in the case of our simulation with no stellar rotation.) This corotation radius should be compared with the radius of the neutral ring (= the inner radius of the disk) r_0 where the disk material is transferred to the magnetospheric field through the magnetic reconnection, because the relative position determines the direction of the angular momentum transfer between the Keplerian disk and the star. Hereafter we concentrate our discussion on the case in which the corotation radius is larger than the radius of the neutral ring and thus

the angular momentum is transferred from the disk to the star.

4.1.1 Qualitative Behavior of the System in the Case of a Rotating Star

Here we briefly discuss the qualitative behavior of the system in the case of a rotating star.

First we consider the motion of the accreting material, which will not differ from the case of no stellar rotation qualitatively. As the disk material is transferred to the magnetosphere through the magnetic reconnection, it is magnetically synchronized with the stellar rotation and becomes sub-Keplerian, since the reconnecting point is assumed to be within the corotation radius. Due to this imbalance between the gravity and the centrifugal force, the material can start falling toward the star along the magnetospheric field and finally accretes to the stellar surface. The excess angular momentum is loaded on the reconnected line of force and is redistributed through the magnetic stress.

Next we consider the motion of the jet. We assume that the Alfvén radius of the star is large enough. (Here we define the Alfvén radius of the star as the radius within which the jet flow is sub-Alfvénic, or passive to the open magnetic field of the star and thus affected by the stellar rotation through the magnetic stress. Beyond the Alfvén radius the jet material does not interact with the star so much and almost performs a ballistic motion conserving its angular momentum.) Within the Alfvén radius, the reconnected stellar-polar field lines are quickly synchronized with the stellar rotation compared with the jet motion (because the jet is “sub-Alfvénic”). Then the jet is also synchronized with the stellar rotation and coasts along the open field lines which rotate almost rigidly with the star out to the Alfvén radius. In

the actual case, this synchronizing motion may be a non-steady one like Draine (1983), or Uchida and Shibata (1985). To examine these magneto-centrifugal effect, however, we adopt the steady centrifugal wind model for simplicity. In the cold limit, the initial acceleration is needed for the wind material to reach the region where the gradient of the effective potential in the corotating frame Φ_{eff} is directed outward and thus the magneto-centrifugal acceleration is possible (Figure 4.1). The effective potential is written as follows.

$$\begin{aligned}\Phi_{eff}(r, z) &= -\frac{GM}{(r^2 + z^2)^{\frac{1}{2}}} - \frac{1}{2}\Omega^2 r^2 \\ &= -\frac{GM}{r_c} \left[\frac{1}{2} \left(\frac{r}{r_c} \right)^2 + \frac{r_c}{(r^2 + z^2)^{\frac{1}{2}}} \right],\end{aligned}\quad (1)$$

where Ω is the angular velocity of the corotating frame and r_c is the corotation radius defined as,

$$\Omega^2 \equiv \frac{GM}{r_c^3}.\quad (2)$$

In the breaking-up star model (Shu et al. 1989), the material is accelerated magneto-centrifugally along the open stellar field lines from the corotating point (X point) which coincides with the interface between the star and the disk, and thus little acceleration is needed initially. (But the question may be on the occurrence of the stellar breaking up itself or the corotation of the open field lines with the star which are no longer rooted to the star.) The same advantage of the shallow potential will be expected in models of the magneto-centrifugal wind from the Keplerian disk, because all field lines are rooted to the local corotation points. (Blandford and Payne 1982, Königl 1989).

In the model using the rotation of the non breaking-up star like our case, if

the material is supplied from the point within the corotation point in the equatorial plane, a considerable initial acceleration is needed for the material to pass over the "ridge" of the effective potential surface and be accelerated magneto-centrifugally along the fields lines rooted to the star (Figure 4.1). In our situation this is accomplished by the acceleration associated with the magnetic reconnection. Beyond the "ridge" of the effective potential, the jet material can be further accelerated magneto-centrifugally, and thus the star suffers the magnetic braking.

Another effect of the stellar rotation will be the deformation of the magnetic field configuration of the star. The hoop stress by the toroidal component of the open fields generated by the stellar rotation will contribute to the collimation of the magneto-centrifugal jet (Blandford and Payne 1982, Sakurai 1985).

4.1.2 The Effect on the Angular Momentum Transfer

We consider here the angular momentum transfer along one reconnected open field line. (The process discussed below will occur continuously on successive axisymmetrical flux surfaces). We assume that the carriers of the angular momentum are only the star and the disk material, and the latter is splitted into the accreting material and the jet material. (i) In the initial state, just after the reconnection, the star whose moment of inertia is I , rotates at the angular velocity Ω , and the transferred material δm_d rotates at the Keplerian angular velocity $\Omega_K(r_0)$ at the reconnecting point $r = r_0$. (ii) In the final state, a part (δm_a) of the disk material accretes on the stellar surface R_* and another part (δm_j) is magneto-centrifugally accelerated out to the Alfvén radius r_A . The star, the accreting material δm_a , and the jet material δm_j , are all assumed to be synchronized and corotating at the stellar angular veloc-

ity $\Omega_* + d\Omega$, by the magnetic action. Then the angular momentum conservation is written as follows. (cf. Shu et al. 1988, Lamb 1989)

$$I_*\Omega_* + \delta m_d r_0^2 \Omega_K(r_0) = (I_* + \delta m_j r_A^2 + \delta m_a R_*^2)(\Omega_* + d\Omega_*), \quad (3)$$

where

$$\delta m_d = \delta m_a + \delta m_j, \quad (4)$$

from which we have

$$d\Omega_* = \frac{\delta m_d r_0^2 \Omega_K(r_0) - \delta m_j r_A^2 \Omega_* - \delta m_a R_*^2 \Omega_*}{I_* + \delta m_j r_A^2 + \delta m_a R_*^2}. \quad (5)$$

Here we do not consider the change of the radius R_* and the moment of the inertia of the star I_* , due to the accretion or due to stellar evolution, for simplicity. The appropriate value of the Alfvén radius r_A makes the steady rotation ($d\Omega_* = 0$) possible, which requires

$$\begin{aligned} \left(\frac{r_A}{R_*}\right)^2 &= 1 + \frac{1}{f} \left(\left(\frac{r_0}{R_*}\right)^2 \frac{\Omega_K(r_0)}{\Omega_*} - 1\right) \\ &= 1 + \frac{1}{f} \left(\left(\frac{r_0}{R_*}\right)^3 \left(\frac{r_c}{R_*}\right)^3 - 1\right), \end{aligned} \quad (6)$$

where

$$f \equiv \frac{\delta m_j}{\delta m_a + \delta m_j}. \quad (7)$$

(See section 4.2.)

4.1.3 The Effect on the Acceleration of the Jet

As discussed in section 3.3, the acceleration mechanisms of the jet in the case of non-rotating star were the poloidal acceleration by $\mathbf{j}_p \times \mathbf{B}_p$ and the toroidal acceleration by $\mathbf{j}_p \times \mathbf{B}_t$, both of which are associated with the propagation of the MHD waves generated through the magnetic reconnection process. (Hereafter we call this process as "reconnection-driven".) In the case of a rotating star, if the Alfvén radius r_A is large enough, the magneto-centrifugal acceleration will continue at larger distances after the reconnection-driven acceleration ceases. In the steady magneto-centrifugal wind model, the terminal velocity of the wind is estimated as

$$v_\infty \sim r_A \Omega_* = \left(\frac{r_A}{R_*}\right) v_*, \quad (8)$$

where v_* is the surface velocity of the stellar rotation (Michel 1969, Pudritz 1985). The terminal velocity of the collimated jet in our model should be modified to this value in the presence of the stellar rotation.

4.1.4 Summary of the Effect of the Stellar Rotation

We summarize the effect of the stellar rotation as follows. After the jet material is accelerated by the "reconnection-driven" mechanism, it will be further magneto-centrifugally accelerated out to the Alfvén radius. If the Alfvén radius is large enough, the latter acceleration will dominate and determine the jet terminal velocity.

Furthermore it will be possible that the jet material finally carries away the positive angular momentum which is the same as that the accreting material give the star to accrete on the stellar surface, and that the star rotates at a constant

angular velocity. (In this discussion we neglect the change of the radius and the moment of inertia of the star due to the accretion or due to stellar evolution for simplicity.)

However, note that also in the case of a rotating star, the magnetic reconnection between the disk field and the magnetospheric field has the following intrinsic meanings and we can say that the jet is "driven by the disk accretion".

(i) A part of the disk is accelerated as a collimated jet through the magnetic reconnection which is driven by the disk accretion. Thus the mass loss rate in the form of the jet \dot{M}_{jet} correlates with the mass accretion rate in the disk \dot{M}_{disk} , which is in contrast with the stellar magneto-centrifugal wind model.

(ii) By the "reconnection-driven" mechanism the disk material is launched beyond the barrier of the effective potential, and thus the magneto-centrifugal acceleration along the open field line of the star is first made possible. But in previous magneto-centrifugal wind models, the initial acceleration was not installed in itself and assumed in an ad manner.

(iii) Due to the compressional MHD waves (or shocks) generated through the magnetic reconnection process, the jet which is otherwise has no heating source will be heated as well as accelerated.

4.2 Applications to the YSO-related Phenomena

Here we discuss what are expected from our model when we take the stellar rotation and other factors into account, and try to see whether the YSO-related phenomena can be explicable.

4.2.1 Outflows from YSOs

Thus far we have argued the situation in the vicinity of YSOs in which the star has a dipole-like magnetosphere and the disk around it is penetrated by a large-scale magnetic field. This situation will be naturally expected when we consider the star formation from the interstellar cloud with a large-scale magnetic field. We have shown that a collimated jet is formed through the magnetic reconnection between the disk field and the magnetospheric field, which will be further accelerated magneto-centrifugally by the effect of the stellar rotation. On the other hand, the untwisting outflow together with the magneto-centrifugal acceleration (Uchida and Shibata 1985) will be formed in the region of the disk penetrated by the large-scale magnetic field where the gas is effectively frozen to the magnetic field.

Then, in our picture, it is predicted that two types of bipolar outflow are formed in the star forming regions, that is, the reconnection-driven jet which comes from the interface between the disk and the magnetosphere of the central star, and the untwisting outflow together with the magneto-centrifugal acceleration from the surface of the extended disk. (We have roughly demonstrated these pictures in the case of high-density disk (Section 3.6).) Here we propose that the reconnection-driven jets correspond to the optical jets, and the untwisting outflows together with the magneto-centrifugal acceleration from the inner part of the disk, and that from the outer part of the disk correspond to the high-velocity neutral winds, and the molecular bipolar outflows, respectively.

(a) Optical Jets

We will examine the general properties of the reconnection-driven jet, and discuss the possibility of the application of it to the optical jet from YSOs.

According to the numerical results, in the case of no stellar rotation the jet material gets the velocity above the local escape velocity at $7 \sim 10 R_*$, which corresponds to $\sim 150 \text{ kms}^{-1}$ in the actual case. But, if we take the rotation of the star into account, the jet will be further accelerated magneto-centrifugally. Since the terminal velocity of the jet in this case is roughly given in equation (8), we could obtain an typical value of the velocity of the optical jets ($v_{\infty} \sim 300 \text{ kms}^{-1}$), if the Alfvén radius r_A extends for $\sim 15 R_*$. Here we assume that the surface velocity of the stellar rotation $v_* \sim 20 \text{ kms}^{-1}$, which is the typical value in the young T Tauri phase.

The collimation of the reconnection-driven jet is fairly good and thus explain the high degree of collimation of the optical jets, because the reconnection-driven jet coasts along the open field lines rooted on the central star, which will be bundled by the hoop stress generated by the stellar rotation.

As for the temperature of the jet, we cannot say anything exact, because we assume the adiabatic approximation in the numerical simulations and initial conditions in our simulation does not reproduce the temperature distribution in the actual case. But we can say that the reconnection-driven jets can be heated by the MHD shocks associated with the change of the magnetic configuration through the magnetic reconnection as discussed in section 3.5. We note that the untwisting outflows from the surface of the extended disk is never heated in such a way. (Uchida and Shibata 1985, Shibata and Uchida 1986).

The total duration of the formation of the optical jets is estimated as $\sim 10^4 \text{ yr}$ from observations (e.g. Mundt et al. (1987)). In our model the reconnection driven jet will continue so long as the reconnection between the magnetospheric fields and disk fields continues, and will cease if closed field lines of the star are all opened up

through the magnetic reconnection. This time scale depends on the reconnection rate. The relation between the reconnection rate $\dot{\Phi}$ and the mass accretion rate \dot{M}_{acc} at the interface is written as follows.

$$\dot{\Phi} = \frac{B_0}{\Sigma} \dot{M}_{acc}, \quad (9)$$

where B_0 is the strength of the large-scale field penetrating the disk and Σ is the surface density of the disk at the reconnecting point. The total magnetic flux of the central star is written as $\Phi_* = \pi B_* R_*^2$, with the strength of the stellar field at the pole B_* and the stellar radius R_* . Then the duration of the magnetic reconnection T is estimated as

$$T = \frac{\Phi_*}{\dot{\Phi}} = \frac{\pi B_* R_*^2 \Sigma}{\dot{M}_{acc} B_0}. \quad (10)$$

This means that the duration of the reconnection-driven jet depends on the mass loaded on unit flux tube penetrating the disk Σ/B_0 . If we take conventional values, $B_* \sim 10^{3.5}$ G, $R_* \sim 10^{11.5}$ cm, $\dot{M}_{acc} \sim 10^{-7} M_\odot \text{yr}^{-1}$, $\Sigma \sim 10^3 \text{gcm}^{-2}$ and $B_0 \sim 10^{-1}$ G, we get $T \sim 10^5$ yr for the duration of the magnetic reconnection or the reconnection-driven jet, which is long enough to explain the duration of the formation of the optical jets. (In our simulation, the parametric range concerning the mass loaded on unit flux tube and the field distributions in the disk are limited from practical reasons, so the relation between the reconnection rate and the mass accretion rate will differ from that in the actual case.)

Some optical jets show the intermittence of the mass ejection, which suggest non-steady jet formation (Bührke et al. (1988), Reipurth(1989), Hartigan et al. (1990)). In our model of the reconnection-driven jet, the jet material loaded on a field

line is ejected through the magnetic reconnection in a time-dependent manner. So, if the reconnection occurs intermittently, the reconnection-driven jet is also ejected intermittently, even if the accretion rate in the disk is constant. (The accreting mass is stored at the neutral ring when the magnetic reconnection does not occur.) Here, we mention the possibility of the intermittency of the magnetic reconnection. Some kinds of current-driven instabilities which induce the anomalous resistivity (such as Lower Hybrid Drift Instability) have a threshold value for its occurrence that may lead to the intermittent reconnection. Other possibility is the formation of magnetic islands in the neutral sheet, which will obstruct the meeting of the oppositely-directed field lines.

To the above extent, we consider that the reconnection-driven jets in our model can explain the properties of the optical jets pretty well.

(b) High-Velocity Neutral Winds and Molecular Bipolar Outflows

We consider that both the high-velocity neutral winds and the molecular bipolar outflows are untwisting outflows together with the magneto-centrifugal acceleration from the surface of the extended disk around YSOs, and their origins are different corresponding to their typical velocities. Shibata and Uchida (1986) showed that the typical velocity of the untwisting outflow is $(1 \sim 2) v_K$, where v_K is the Keplerian velocity at its origin. If we apply this to the observational values, then we can estimate that the molecular bipolar outflows ($\sim 20 \text{ km s}^{-1}$) are formed at a larger radius ($\sim 10 \text{ AU}$), while high-velocity neutral winds ($\sim 200 \text{ km s}^{-1}$) are formed in the inner region of the disk ($\sim 0.01 \text{ AU}$) (we assume the central star of 10^{33} g), which naturally explains that the molecular bipolar outflows are less collimated than the high-velocity neutral winds. In our model, the origin of the high-velocity neutral

winds is close to that of the optical jets, but the high-velocity neutral winds will be “cooler” than the optical jet, because the former are not heated in their formation process (see section 3.5).

(c) T Tauri winds

T Tauri winds are identified only by the spectral profiles of forbidden lines [SII] or [OI] and recent high spectral resolution observations suggest that they have complicated structures rather than the simple spherical structure, as discussed in section 1.1. Here in our model, we consider that forbidden line emissions may originate from the unresolved base part of collimated optical jets and/or that of extended high-velocity winds. Since both outflows have the effect of the magneto-centrifugal acceleration in our model, they have rotational velocities comparable to their poloidal velocities around the Alfvén point, which may contribute the complication of forbidden line profiles.

4.2.2 Angular Momentum Problem

Another significant problem concerning the YSOs, especially CTTSs, is the angular momentum problem. Edwards et al. (1993b) studied the statistics of the rotation periods of T Tauri stars and showed that those stars which are surrounded by circumstellar disks have rotation periods $P_{rot} \sim 8.5$ day which is much below the break-up speed, and many of those which are not surrounded by the circumstellar disk have rotation periods $P_{rot} < 4$ day. They suggested that the circumstellar disk regulates the angular velocity of the star at a low rate, or removes the angular momentum from the star. If there exists no mechanism for removing angular mo-

mentum, CTTSs accreting the material of high angular momentum from the disk (typically at the rate $10^{-7} M_{\odot} \text{yr}^{-1}$) will get half of breakup speeds within $\sim 10^6$ yr, which is comparable to the ages of CTTSs (Hartmann and Stauffer 1989, Durisen et al. 1989).

Magnetic action could be the most likely mechanism for removing angular momentum. Königl (1991) applied the model for accreting neutron stars proposed by Ghosh and Lamb (1979) to CTTS case. In their model the coupling between the magnetosphere and the resistive disk may lead to the balance between the positive torque by those penetrating the disk within the corotation radius and the negative torque by the magnetospheric fields penetrating the disk out of the corotation radius. This sounds plausible, but it will not be able to explain the outflows which are the most characteristic phenomena in the disk accretion phase, because all the field lines of the star are closed and penetrate the disk in their model.

In the present paper, we considered another way for removing angular momentum from the rotating star, that is, the magnetic braking by the open field lines rooted to the star. In our model taking the stellar rotation into account, a part of the disk material transferred to the open, reconnected field lines forms a reconnection-driven jet which will be further accelerated magneto-centrifugally and thus can carry off significant angular momentum. (The initial acceleration, which is difficult to attain in the previous models of the magneto-centrifugal wind in the cold limit, is accomplished by the “reconnection-driven” mechanism.)

As discussed in section 4.2, the positive torque by the disk accretion can be canceled by the negative torque by the magneto-centrifugally driven jet and thus constant angular velocity of the star is possible, if the Alfvén radius has an appropriate value. Now we estimate the value of the Alfvén radius needed for such

steady state from equation (6). We need values of the corotation radius r_c , the radius of the reconnecting point r_0 and the ratio of mass loss rate to mass accretion rate f .

If we adopt plausible values, $R_* \sim 10^{11.5}$ cm, $M_* \sim 10^{33}$ g and $v_* \sim 20$ km s⁻¹, we get the corotation radius $r_c \sim 4 R_*$, from the equation (2) in section 1.2.2. We assume that the radius of the neutral ring r_0 , which coincides with the inner edge of the disk, has an almost constant value in its accretion phase. (This would be justified because the magnetic flux brought by the disk accretion per unit time is much smaller than the total magnetic flux of the star. See equation (10).) As discussed in section 1.4 and 3.2, r_0 should be order of several times of the stellar radii, but the exact value will depend on the complicated interaction between the disk accretion and the magnetosphere. Here we adopt the value smaller than r_c , for example, $r_0 \sim 3 R_*$. (The dependence of r_A/R_* on r_0/R_* is small compared with other parameters, r_0/R_* and f (see equation (6)).) As for f , we adopt $f \sim 0.1$ from the observational facts and our numerical results.

Using these values, we get, from equation (6), $r_A \sim 11 R_*$. This value agrees considerably well with the value which is derived in section 4.2.1 for explaining the typical velocity of the optical jets as a terminal velocity of a magneto-centrifugal wind. This means that if the optical jets are finally accelerated magneto-centrifugally to acquire the observed velocity, $200 \sim 400$ km s⁻¹, then it will give the negative torque to the star which cancels the positive torque by the disk accretion at a rate of $10^{-7} M_\odot \text{yr}^{-1}$. So it is possible to explain the constant rotation of YSOs in the disk accretion phase, as a result of the formation of the reconnection-driven jet (the optical jets) which is further accelerated magneto-centrifugally.

After the disk accretion phase ceases, it is plausible that the star spins up,

conserving its angular momentum, due to the change of the moment of inertia which comes from the contraction of the star or the change of the internal structure in the T Tauri star evolution, as proposed in Edwards et al. (1993b). But, to be exact, the star cannot conserve its angular momentum if the accretion ceased, because it will interact with the ambient medium and loses its angular momentum through the open field lines, if they exist. (The rate of the angular momentum loss will be much smaller than that in the jet formation phase.) In our model, when the accretion ceases and no more stress acts on the magnetosphere of the star, then the configuration of magnetic fields begins to change to that of the potential field. This means that the field lines opened up by the magnetic reconnection close through the reverse reconnection process and the angular momentum loss along open field lines is reduced. Thus, the change of the configuration of the magnetic field helps the star to spin up, and is consistent with the result of Edwards et al. (1993b).

Chapter 5

Summary and Overall Discussion

– The Dynamical Role of Magnetic Fields in the Whole Star Formation Process –

Now we can construct a rough scenario of the star formation process taking into account the large-scale magnetic fields initially penetrating the interstellar cloud. The large-scale magnetic field plays an important role on the dynamical evolution of the system, especially on the formation of energetic outflows.

A cloud core collapses by the gravitational instability and forms a protostar and the surrounding protostellar disk. Since the angular momentum component normal to the large-scale magnetic field is removed more efficiently than the parallel component (Mestel 1965, Mouschovias and Paleologou 1980) in the earlier phases, the surrounding protostellar disk is penetrated by the large-scale magnetic field which is parallel with the rotational axis.

The angular momentum of the disk is carried off along the large-scale magnetic field twisted up by the disk rotation, which leads to the enhancement of the disk accretion. Furthermore if the toroidal fields are generated amply enough, the unwinding of them pushes upward the material of the surface layers of the disk to form spinning bipolar outflows. In this case the extraction of angular momentum from the disk is more efficient through both the magnetic stress and the material stress.

This untwisting outflow formed at relatively large radius (≥ 10 AU) of the disk may correspond to the CO molecular bipolar outflows (20 km s^{-1}) (Uchida and Shibata 1985, Shibata and Uchida 1986). Uchida et al. (1987a, 1987b) observationally verified the spinning of the molecular bipolar outflow in L1551, which is considered to be the result of the angular momentum transfer from the rotating disk to the outflow via the large-scale magnetic field. The untwisting outflow may also be formed at the inner part of the disk (~ 0.01 AU), and accelerated more energetically, deeper in the gravitational potential, which may correspond to the high-velocity neutral wind ($\sim 200 \text{ km s}^{-1}$).

The field configurations in the vicinity of young stars are such as follows (Uchida and Shibata 1984, 1985): Although most of initial magnetic flux of the cloud are lost through its collapse by the ambipolar diffusion or the Ohmic diffusion in the earlier phase, the stellar core brings in significant amount of the flux and acquires a dipolar magnetosphere (Uchida and Low 1981). The magnetosphere will have the field strength of $\sim 10^3$ G at the pole (Nakano and Umebayashi (1986)) and truncate the accretion disk at a distance of several stellar radii. The inner edge of the disk coincides with the magnetically neutral ring in the equatorial plane, because the disk is penetrated by the large-scale magnetic field whose direction is the same as the stellar dipole moment. (This is because both magnetic fields are originated from the same interstellar magnetic fields.) The disk accretion drives the magnetic reconnection between the closed magnetospheric field and the disk field, and then the mass and the angular momentum are transferred from the disk to the magnetosphere of the star. Yusef-Zadeh et al. (1990) detected synchrotron emission from a HH-like object in Orion by VLA observations. From the large-scale linearly polarized stellar emission, they suggest the magnetic reconnection in the outer mag-

netosphere of the central star along the equatorial region, which is consistent with our picture (Uchida and Shibata 1984).

If the inner radius of the disk is smaller than the corotation radius, the transferred material is magnetically braked by the star and most of it falls toward the stellar surface. In this case, the final accretion onto the YSO will be guided by the magnetospheric field and the gravitational energy of the disk material is liberated when it crashes at the stellar surface (Uchida and Shibata 1984), because the accretion disk is truncated at several stellar radii and is not in direct contact with the stellar surface (that is, the "boundary layer" does not exist). Bertout et al. (1988) showed the light curve of a T Tauri star which suggests the hotspot corresponding to the crashing of the guided flow at the stellar surface.

The magnetic reconnection changes the topology of the magnetic field and the flux of the disk field is not brought into the central star, while most of the materials of the accretion disk are added to the star. The amount the magnetic flux brought into the star is determined when the stellar core is formed, and not later.

We have demonstrated in 2.5-dimensional MHD simulations in which a collimated jet is formed through the magnetic reconnection between the disk field and the magnetospheric field in association with the final accretion process ("reconnection-driven jet") in the case of no stellar rotation. We consider that this highly collimated jet along the open stellar field lines corresponds to the optical jets. This jet is accelerated by the Lorentz force through the propagation of the MHD waves associated with the relaxation of the magnetic field distorted through the magnetic reconnection. The ultimate source of the energy of the jet in this case is the released gravitational energy of the disk material: The inward accretion builds up the toroidal current, and the magnetic energy of the poloidal field around the magneti-

cally neutral ring, which is converted to the energy of the jet through the magnetic reconnection. On the other hand, since the reconnected lines of force have been distorted by the rotational velocity shear near the reconnection point, the rotational energy of the accreting material is stored as the magnetic energy of the toroidal field, which is also converted to the energy of the jet through the magneto-centrifugal acceleration.

The effects of the stellar rotation will be summarized as follows: If the Alfvén radius is large enough, the jet matter is synchronized with the stellar rotation through the magnetic action and then further accelerated magneto-centrifugally. In this case, a substantial fraction of the energy of the jet comes from the rotational energy of the central star. However, the "reconnection-driving" is intrinsically important in the initial acceleration needed for the magneto-centrifugal acceleration, and also in relating the mass loss rate by the jet with the mass accretion rate in the disk. Another important effect of the stellar rotation is the angular momentum loss by the jet which is accelerated magneto-centrifugally. We have shown that the relatively low and constant rotation rate of CTTs in disk accretion phase (Edwards et al. 1993b) can be explained by the angular momentum loss in the formation of the reconnection-driven jets (the optical jets) which are finally accelerated magneto-centrifugally by the stellar rotation.

HH objects are now considered to result from the interaction of the high-velocity jets from YSOs with the ambient medium. In our picture, the accelerated jet propagates along the stellar open field which is twisted by the stellar rotation (Uchida et al. 1992). Todo et al. (1992a, 1992b) have performed 2.5 and 3-dimensional MHD simulations of the jet propagation in the helical magnetic fields and showed that the wiggled structures of some HH objects can be reproduced by the helical-kink

instability driven by the intensified toroidal fields in MHD shocks.

After the disk accretion ceased, the configuration of the magnetic field changes to that of the current-free field. When the circumstellar region is evacuated and the rarefied plasma can not sustain necessary current in it, the field lines opened up by the magnetic reconnection are re-closed through the reverse magnetic reconnection. The reverse reconnection reduces the angular momentum loss along the open field lines, and helps the star in the final contracting phase to spin up, as shown by Edwards et al. (1993b).

References

- Adams,F.C., Lada,C.J., and Shu,F.H. 1987, *Astrophys.J.*, **312**, 788.
- André,Ph., Phillips,R.B., Lestrade,J.-F., and Klein,K.L. 1991, *Astrophys.J.*, **376**, 630.
- Appenzeller,I. 1983, *Rev.Mexicana Astron.Astrophys.*, **7**, 41.
- Appenzeller,I., Jankovics,I., and Ostreicher,R. 1984, *Astron.Astrophys.*, **141**, 108.
- Arons,J. 1993, *Astrophys.J.*, **408**, 160.
- Bertout,C., Basri,G., and Bouvier,J. 1988, *Astrophys.J.*, **330**, 350.
- Blandford,R.D., and Payne,D.G. 1982, *Monthly Notices Roy.Astron.Soc.*, **199**, 883.
- Bürke,T., Mundt,R., and Ray,T.P. 1988, *Astron.Astrophys.*, **200**, 99.
- Camenzind,M. 1990, *Rev.Modern Astron.*, **3**, 234.
- Cabrit,S., Edwards,S., Strom,S.E., and Strom,K.M. 1990, *Astrophys.J.*, **354**, 687.
- Calvet,N., and Canto,J., and Rodriguez,L.F. 1983, *Astrophys.J.*, **268**, 739.
- De Campli,W.M., 1981, *Astrophys.J.*, **244**, 124.
- Draine,B.T., 1983, *Astrophys.J.*, **270**, 519.
- Durisen,R.H., Yang,S., Cassen,P.,and Stahler,S.W. 1989, *Astrophys.J.*, **345**, 959.
- Edwards,S., and Snell,R.L. 1982, *Astrophys.J.*, **261**, 151.
- Edwards,S., Cabrit,S., Strom,S., Heyer,I., Strom,K., and Anderson,E. 1987, *Astrophys.J.*, **321**, 473.
- Edwards,S., Ray,T., and Mundt,R. 1993a, in *Protostars and Planets III*, eds.E.H.Levy and J.I.Lunine (Tucson : University of Arizona Press), p567.
- Edwards,S., Strom,S.E., Hartigan,P., Strom,K.M., Hillenbrand,L.A., Herbst,W., Attridge,J., Merrill,K.M., Probst,R., and Gatley,I. 1993b, *Astron.J.*, **106**, 372.
- Fukui,Y., Iwata,T., Mizuno,A., Bally,J., and Lane,A.P. 1993, in *Protostars and Plan-*

- ets III, eds.E.H.Levy and J.I.Lunine (Tucson : University of Arizona Press), p603.
- Ghosh,P., and Lamb,F.K. 1979, *Astrophys.J.*, **232**, 259.
- Hartmann,L., Edwards,S., and Avrett,A. 1982, *Astrophys.J.*, **261**, 279.
- Hartmann,L., and McGregor,K.B., 1982, *Astrophys.J.*, **259**, 180
- Hartmann,L., and Stauffer,J., 1989, *Astron.J*, **97**, 874.
- Hartigan,P., Raymond,J., and Meaburn,J. 1990, *Astrophys.J.*, **362**, 624.
- Hayashi,M., Ohashi,N., and Miyama,S.M. 1993, *Astrophys.J.*, **418**, L71
- Hoshino,M. 1991, *J.Geophys.Res.*, **96**, 11555.
- Huba,J.D., Gladd,N.T., and Papadopoulos,K. 1978, *J.Geophys.Res.*, **88**, 6926.
- Koo,B.-C. 1989, *Astrophys.J.*, **337**, 318.
- Koo,B.-C. 1990, *Astrophys.J.*, **361**, 145.
- Königl,A. 1982, *Astrophys.J.*, **261**, 115.
- Königl,A. 1989, *Astrophys.J.*, **342**, 208.
- Königl,A. 1991, *Astrophys.J.*, **370**, L39.
- Kwan,J., and Tademaru,E. 1988, *Astrophys.J.*, **332**, L41.
- Lada, C.J., 1985, *Ann.Rev.Astron.Astrophys.*, **23**, 267.
- Lago,M.T.V.T. 1984, *Monthly Notices Roy.Astron.Soc.*, **210**, 323.
- Lamb,F.K. 1989, in *Timing Neutron Stars*, eds.H.Ogelman and E.P.J.van den Heuvel (Dordrecht: Kluwer), p649.
- Lavreault,R.M. 1988, *Astrophys.J.*, **330**, 897.
- Lizano,S., Heiles,C., Rodriguez,L.F., Koo,B.-C., Shu,F.H., Hasegawa,T., Hayashi, S.S., and Mirabel,I.F. 1988, *Astrophys.J.*, **328**, 763.
- Lovelace,R.V.E., Berk,J.L., and Contopoulos,J. 1991, *Astrophys.J.*, **379**, 696.
- Low,B.C. 1984, *Astrophys.J.*, **281**, 381.
- Mestel,L. 1965, *Quart.J.Roy.Astron.Soc.*, **6**,161.
- Michel,F.C. 1969, *Astrophys.J.*, **158**, 727.
- Mitchell,G.F., Allen,M., Beer,R., Dekany,R., Huntress,W., and Maillard,J.-P. 1988a, *Astron.Astrophys.*, **201**, L16.
- Mitchell,G.F., Allen,M., Beer,R., Dekany,R., Huntress,W., and Maillard,J.-P. 1988b, *Astrophys.J.*, **327**, L17.
- Mitchell,G.F., Curry,C., Maillard,J.-P. and Allen,M. 1989, *Astrophys.J.*, **341**, 1020.
- Montmerle,T., Feigelson,E.D., Bouvier,J., and André,P. 1993, in *Protostars and Planets III*, eds.E.H.Levy and J.I.Lunine (Tucson : University of Arizona Press), p689.
- Mouschovias,T., and Paleologou,E.V. 1980, *Astrophys.J.*, **237**, 877.
- Mundt,R., and Fried,J.W. 1983, *Astrophys.J.Letters*, **274**, L83.
- Mundt,R., Brugel,E.W., and Bührke,T. 1987, *Astrophys.J.*, **319**, 275.
- Mundt,R., Ray, T.P., Buhrke, T., Raga, A.C., and Solf, J., 1990, *Astron.Astrophys.*, **232**, 37.
- Nakano,T., and Umabayashi,T. 1986, *Monthly Notices Roy.Astron.Soc.*, **221**, 319.
- Nakano,T. 1991, *Mem.Soc.Astr.Ital.*, **62**, 841.
- Petechek,H.E. 1964, in *AAS-NASA symposium on the Physics of Solar Flares*, ed.W.N.Hess, NASA SP-50, p425.
- Pringle,J.E. 1989, *Monthly Notices Roy.Astron.Soc.*, **236**, 107.
- Pringle,J.E., and Rees,M.J. 1972, *Astron.Astrophys.*, **21**, 1.
- Pudritz,R.E. 1985, *Astrophys.J.*, **293**, 216.
- Pudritz,R.E., and Norman,C.A. 1983, *Astrophys.J.*, **274**, 677.
- Pudritz,R.E., and Norman,C.A. 1986, *Astrophys.J.*, **301**, 571.
- Pudritz,R.E., Pelletier,G., and Gomez de Castro,A.I. 1991, *The Physics of Star For-*

- mation and Early Stellar Evolution*, eds.C.J.Lada and N.D.Kylafis (Kluwer Academic Publishers, Printed in the Netherlands), p539.
- Raga,A.C., and Canto,J. 1989, *Astrophys.J.*, **344**, 404.
- Raga,A.C., Canto,J., Binette,L., and Calvet,N. 1990, *Astrophys.J.*, **364**, 601.
- Reipurth,B. 1989, *Nature*, **340**, 42.
- Richtmyer,R.D., and Morton,K.W. 1967, *Difference Methods for Initial-Value Problems* 2nd ed. (Interscience Publishers, New York), Chap. 13.
- Rubin,E.L., and Burstein,S.Z. 1967, *J.Comp.Phys.*, **2**, 178.
- Sato,T., and Hayashi,T. 1979, *Phys.Fluids*, **22**, 1189.
- Sakurai,T. 1987, *Publ.Astron.Soc.Japan*, **152**, 121.
- Shakura,N.I., and Sunyaev,R.A. 1973, *Astron.Astrophys.*, **24**,337.
- Sargent,A.I., and Beckwith,S. 1987, *Astrophys.J.*, **323**, 294.
- Sargent,A.I., and Beckwith,S. 1991, *Astrophys.J.*, **382**, L31.
- Shibata,K., and Uchida,Y. 1986, *Publ.Astron.Soc.Japan*, **38**, 631.
- Shu,F.H., and Terebey,S. 1984, in *Cool Stars, Stellar Systems and the Sun*, eds.S.Baliunas and L.Hartmann (Berlin:Springer Verlag) p78.
- Shu,F.H., Adams,F.C., and Lizano,S. 1987, *Ann.Rev.Astron.Astrophys.*, **25**, 23.
- Shu,F.H., Lizano,S., Ruden,S.P., and Najita,J. 1988, *Astrophys.J.*, **328**, L19.
- Snell, R.L., Loren, R.B., and Plambeck, R.L., 1980, *Astrophys.J.Letters*, **239**, L17.
- Strittmatter,P.A. 1965, *Monthly Notices Roy.Astron.Soc.*, **132**, 359.
- Strom,K.M., Strom,S.E., Wolff,S.C., Morgan,J., and Wenz,M. 1986, *Astrophys.J.Suppl.*, **62**, 39.
- Todo,Y., Uchida,Y., Sato,T., and Rosner,R., 1992, *Publ.Astron.Soc.Japan*, **44**, 245.
- Todo,Y., Uchida,Y., Sato,T., and Rosner,R., 1992, *Astrophys.J.*, **403**,164.
- Torbett,M.V. 1984, *Astrophys.J.*, **278**, 318.
- Uchida,Y., and Low,B.C. 1981, *J.Astrophys.Astron.*, **2**, 405.
- Uchida,Y., Kaifu,N., Shibata,K., Hayashi,S.S., and Hasegawa,T. 1987a, in *Star-Forming Regions*, ed. Peimbert,E.and Jugaku,J. (Reidel), p285.
- Uchida,Y., Kaifu,N., Shibata,K., Hayashi,S.S., Hasegawa,T., and Hamatake,H. 1987b, *Publ.Astron.Soc.Japan*, **39**, 907.
- Uchida,Y., and Shibata,K. 1984, *Publ.Astron.Soc.Japan*, **36**, 105.
- Uchida,Y., and Shibata,K. 1985, *Publ.Astron.Soc.Japan*, **37**, 515.
- Uchida,Y., Todo,Y., Rosner,R., and Shibata,K. 1992, *Publ.Astron.Soc.Japan*, **44**, 227.
- Uchida,Y. 1986, in *Low Mass Star Formation and Protostellar Objects*, ed.B.Reipurth (ESO publications), p141.
- Ugai,M., and Tsuda,T. 1977, *J.Plasma Phys.*, **17**, 377.
- Umebayashi,T., and Nakano,T. 1988, *Prog.Theor.Phys.Suppl.*, **96**, 151.
- Yusef-Zadeh,F., Cornwell,T., Reipurth,B., and Roth,M. 1990, *Astrophys.J.*, **348**, L61.

Acknowledgement

The author would like to express his sincere thanks to Professor Y.Uchida. His valuable advice and continuous encouragement was a great help in completing this work. The author is indebted to Dr. K.Shibata for many illuminating discussion on the results of the numerical simulations. To Dr. M.Hayashi he owes thanks for discussion on the observational aspects of the problem. He also thanks Dr. Y.Todo and Dr. R.Matsumoto for many helpful discussions.

Figure Captions

Figure 1.1

(a) Schematic picture of the multiple structure of outflows from a YSO. (b) Schematic picture of the configuration of the magnetic fields around a YSO and the final accretion process onto the YSO in our model.

Figure 2.1

Simulation region; Initial conditions; Boundary conditions.

Figure 3.1

Time evolution of various quantities in the poloidal plane.

- (a) poloidal field line : contours of rA_ϕ , test particles
- (b) density : contours of $\log \rho$, poloidal velocity field : (v_r, v_z)
- (c) poloidal velocity field : (v_r, v_z)
- (d) poloidal field line : contours of rA_ϕ
- (e) density : contours of $\log \rho$
- (f) pressure : contours of $\log p$
- (g) test particles
- (h) temperature : contours of $\log T$
- (i) toroidal velocity : contours of v_ϕ (+ component in the upper part, - component in the lower part)
- (j) toroidal field : contours of B_ϕ (+ component in the upper part, - component

in the lower part)

- (k) current : contours of j_r (+ component)
- (l) current : contours of j_r (- component)
- (m) current : contours of j_ϕ (+ component)
- (n) current : contours of j_ϕ (- component)
- (o) current : contours of j_z (+ component)
- (p) current : contours of j_z (- component)
- (q) entropy : contours of $\log(pp^{-\gamma})$
- (r) beta : contours of $\log \beta = \log(8\pi p/B^2)$
- (s) magnetic pressure : contours of $\log(B^2/8\pi)$
- (t) total pressure : contours of $\log(p + B^2/8\pi)$

Figure 3.2

Time variation of the distribution of the specific angular momentum $rv_\phi/|B_p|$ along a poloidal flux tube penetrating the disk.

Figure 3.3

Magnetic reconnection in three dimensions. Lines of force to be reconnected are drawn at $t=0.0$. The closed lines of force are a part of the magnetosphere, and the surrounding lines of force like an hour-glass are penetrating the disk.

(a) top view, (b) side view, (c) perspective view.

Figure 3.4

(a) Time variation of the radius of the neutral ring r_n . (b) Time variation of

the flux function rA_ϕ at the neutral ring.

Figure 3.5

(a) Distribution of various forces in r - direction in the equatorial plane around the neutral ring. (b) Distribution of various pressures in the equatorial plane around the neutral ring.

Figure 3.6

(a) Motion of a field line rooted to the star which is closed initially. Numbers(1~9) show the time sequence. (b) Time variation of the distribution of the angular momentum $\rho rv_\phi/|B_p|$ along the stellar field line (flux tube) corresponding to (a). (c) Time variation of the distribution of the angular momentum flux $(-\rho rv_\phi v_p \cdot B_p/B_p + rB_\phi B_p/4\pi)/B_p$ along the stellar field line (flux tube) corresponding to (a). (d) Decomposition of the angular momentum flux (c) to the magnetic stress and the material stress at the time 3 and 9.

Figure 3.7

(a) The motion of a particle and the field line which the particle is frozen to. The particle is initially located inside the disk and finally ACCRETES to the star. (b) Time variation of works $\mathbf{F} \cdot \mathbf{v}$ done by various forces acting on the particle, corresponding to (a). (c) Time variation of the specific angular momentum rv_ϕ of the particle, corresponding to (a). 'magnetic braking' shows the work $F_\phi^{Lorentz} v_\phi$ done by the azimuthal component of the Lorentz force.

Figure 3.8

(a) The motion of a particle and the field line which the particle is frozen to. The particle is initially located in the surface layer of the disk and is finally ejected in the JET. (b) Time variation of works $\mathbf{F} \cdot \mathbf{v}$ done by various forces acting on the particle, corresponding to (a). (c) Time variation of works $\mathbf{F} \cdot \mathbf{v}$ done by decomposed Lorentz force acting on the particle, corresponding to (a).

Figure 3.9

Magnifications of the region around the neutral point, (a) poloidal field lines \mathbf{B}_p , toroidal current j_ϕ , (b) poloidal field lines \mathbf{B}_p , poloidal velocity field (v_r, v_z) . (Closed field lines rooted to the star are not drawn.)

Figure 3.10

(a) The motion of a particle and the field line which the particle is frozen to. The particle is initially located in the corona and finally forms the JET and suffers MHD-slow mode SHOCK. (b) Time variation of physical quantities of the test particle. Temperature T , entropy $s = \log(pp^{-\gamma})$. (c) Time variation of physical quantities of the test particle. Gas pressure p , poloidal magnetic pressure $B_p^2/8\pi$, toroidal magnetic pressure $B_\phi^2/8\pi$.

Figure 3.11

Time evolution of various quantities in the poloidal plane in the case of high-density disk. Arrows indicate helical magnetic islands.

(a) poloidal velocity field : (v_r, v_z)

(b) poloidal field line : contours of rA_ϕ

(c) current : contours of j_ϕ (- component)

(d) test particles

(e) toroidal velocity : contours of v_ϕ (+ component in the upper part, - component in the lower part)

(f) toroidal field : contours of B_ϕ (+ component in the upper part, - component in the lower part)

Figure 3.12

Perspective view of a helical magnetic island formed in the secondary reconnection.

Figure 4.1

Contour of the effective potential in the corotation frame. "Ridge" means the potential barrier along field lines rooted to the central star.

	protostar	CTTS	WTTS	observation	scale l (pc)	velocity v (kms $^{-1}$)	dynamical time scale l/v (yr)	mass loss rate \dot{M} ($M_{\odot}\text{yr}^{-1}$)	momentum discharge $\dot{M}v$ ($L_{\odot}c^{-1}$)	kinetic luminosity $\frac{1}{2}\dot{M}v^2$ (L_{\odot})
molecular bipolar outflow	○	△	×	CO	~ 1	~ 20	$\sim 10^{4.5}$	$\sim 10^{-6}$	$\sim 10^2$	$\sim 10^{-1.5}$
high velocity neutral wind	○	?	×	CO, HI	?	~ 200	?	$\sim 10^{-7}$	$\sim 10^2$	$\sim 10^{-0.5}$
optical jet	○	△	×	[OI], [SII]	~ 0.1	~ 200	$\sim 10^{2.5}$	$\sim 10^{-9} - 10^{-8}$	$\sim 10^0 - 10^1$	$\sim 10^{-2.5} - 10^{-1.5}$
T Tauri wind	—	○	×	[OI], [SII]	—	~ 200	—	$\sim 10^{-8} - 10^{-7}$	$\sim 10^1 - 10^2$	$\sim 10^{-1.5} - 10^{-0.5}$

Table 1.1 Summary of the characteristics of outflows from YSOs

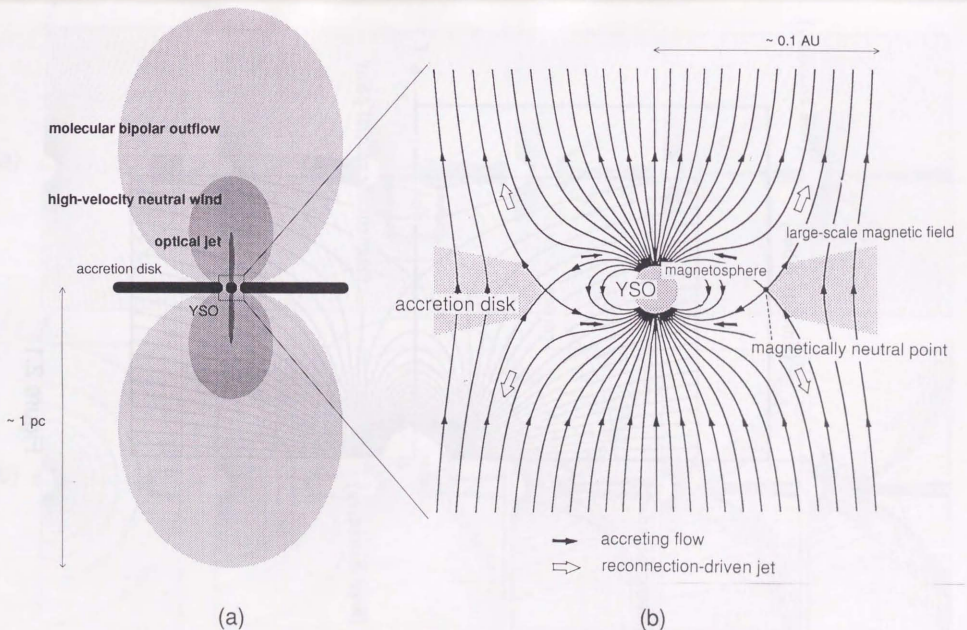


Figure 1.1

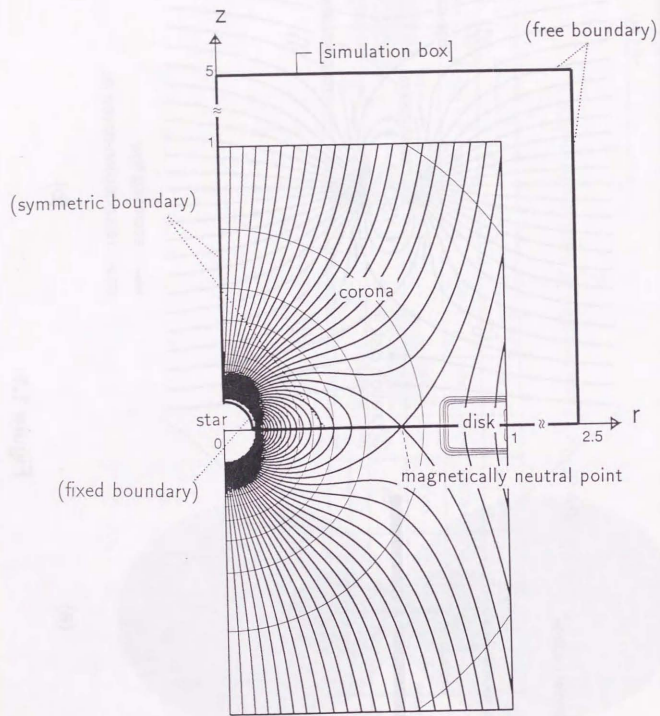


Figure 2.1

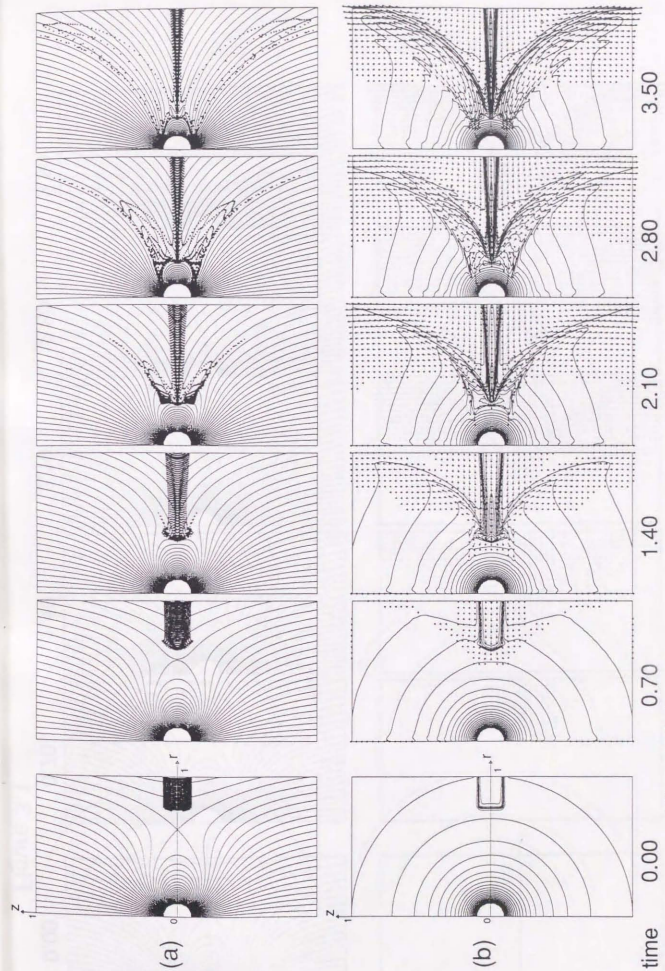


Figure 3.1

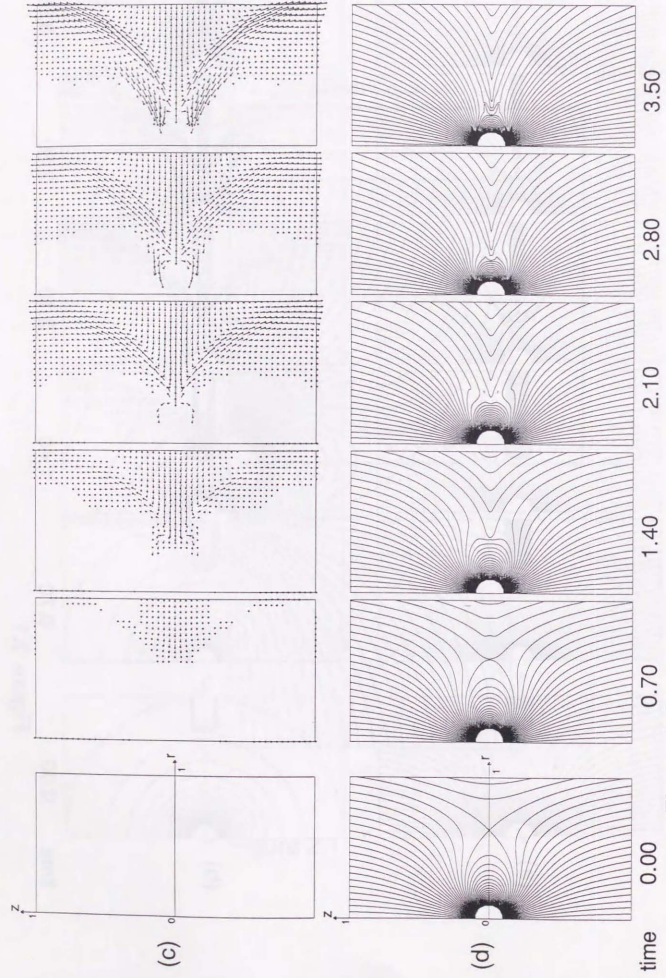


Figure 3.1

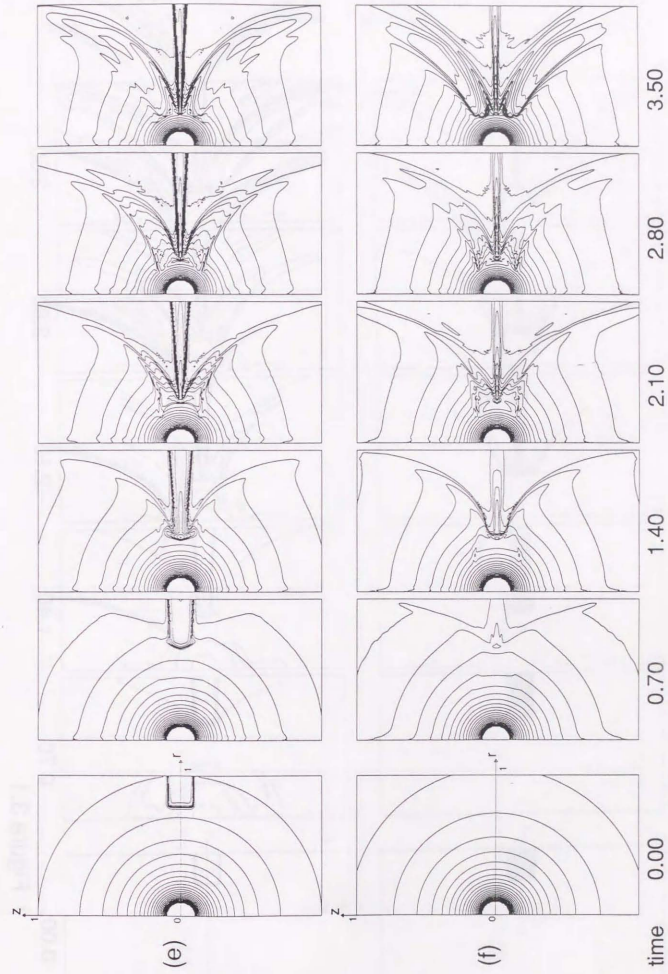


Figure 3.1

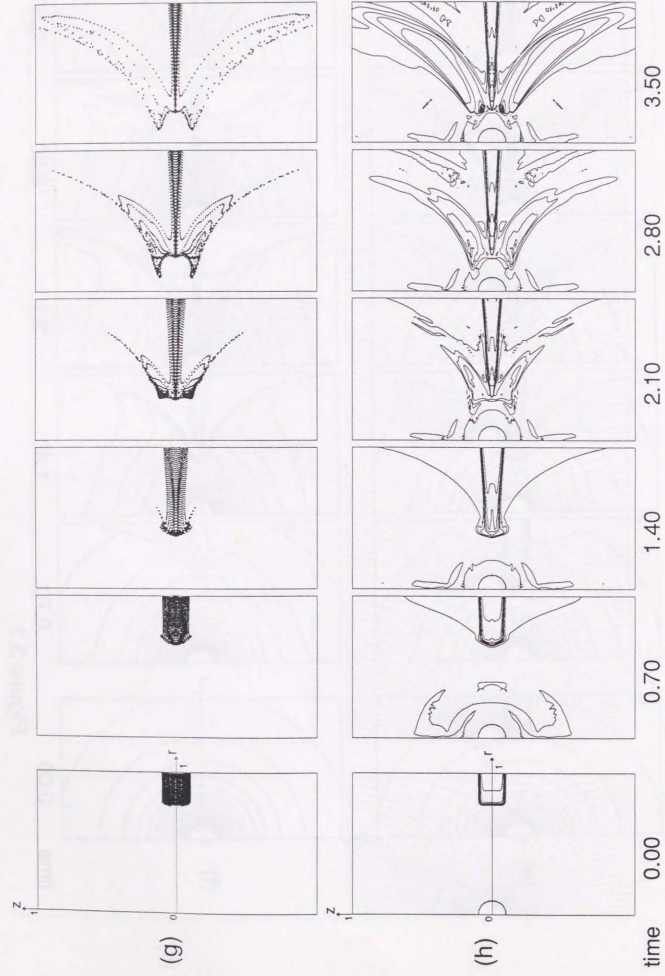


Figure 3.1

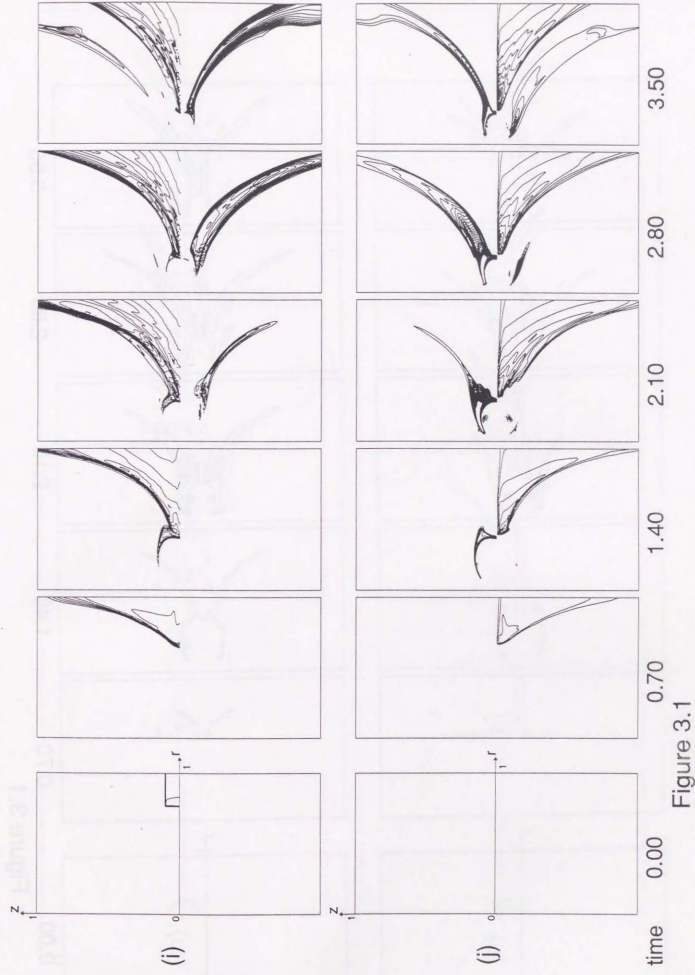


Figure 3.1

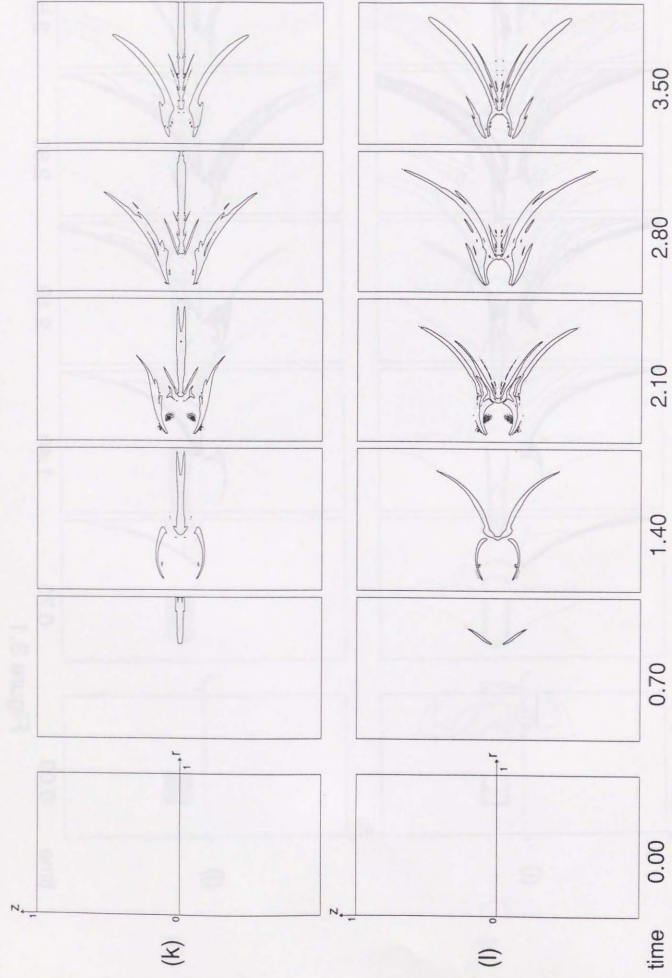


Figure 3.1

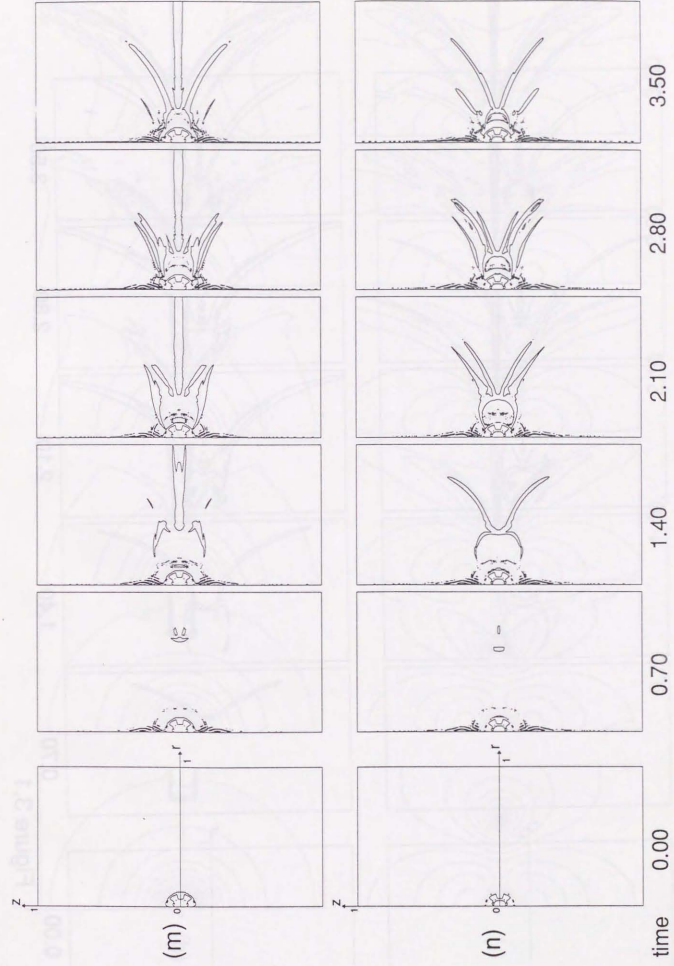


Figure 3.1

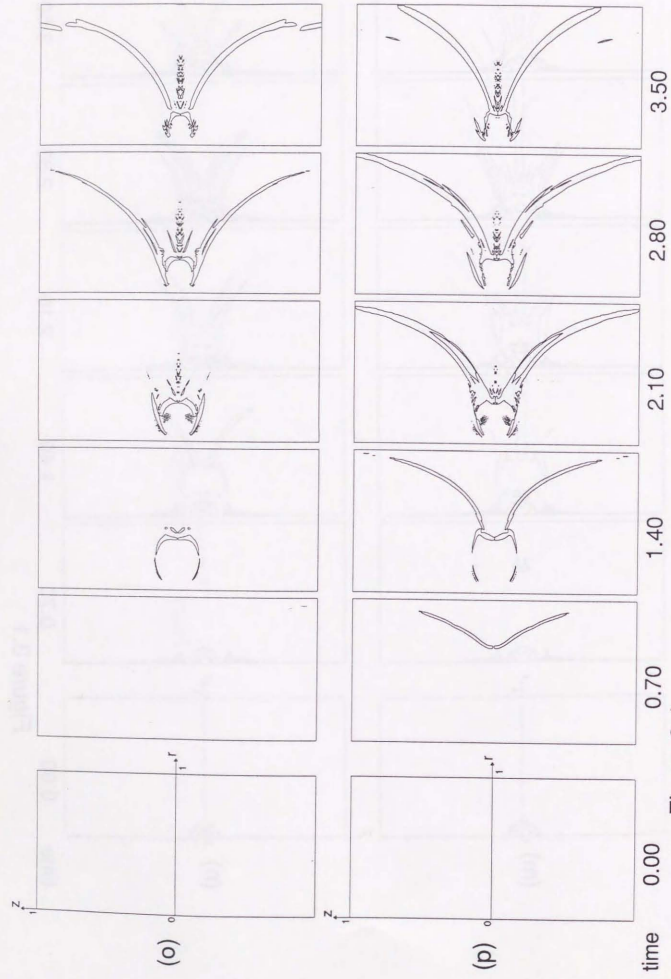


Figure 3.1

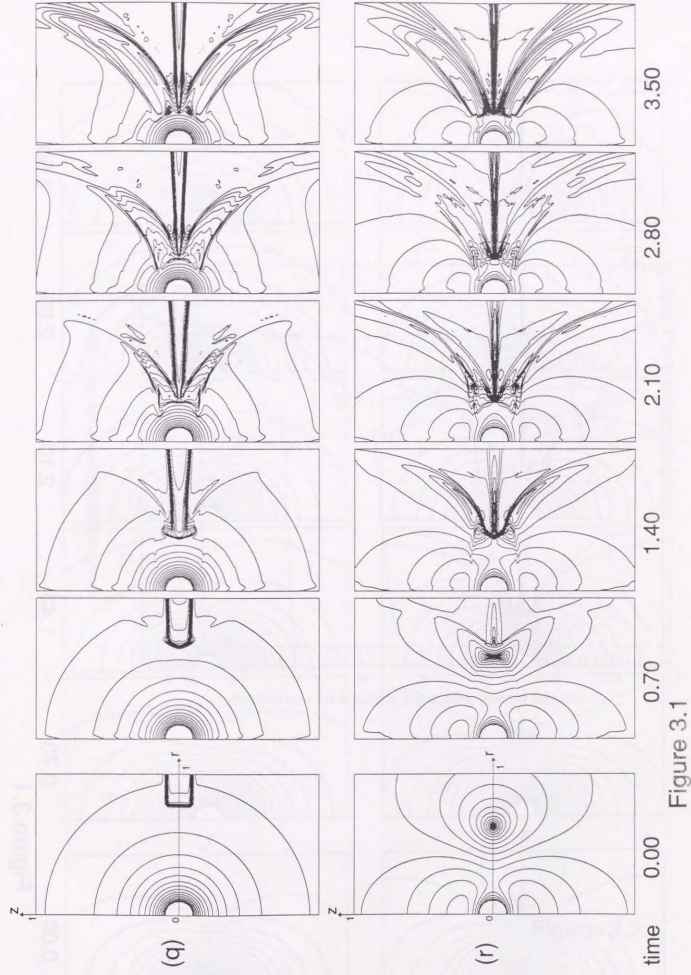


Figure 3.1

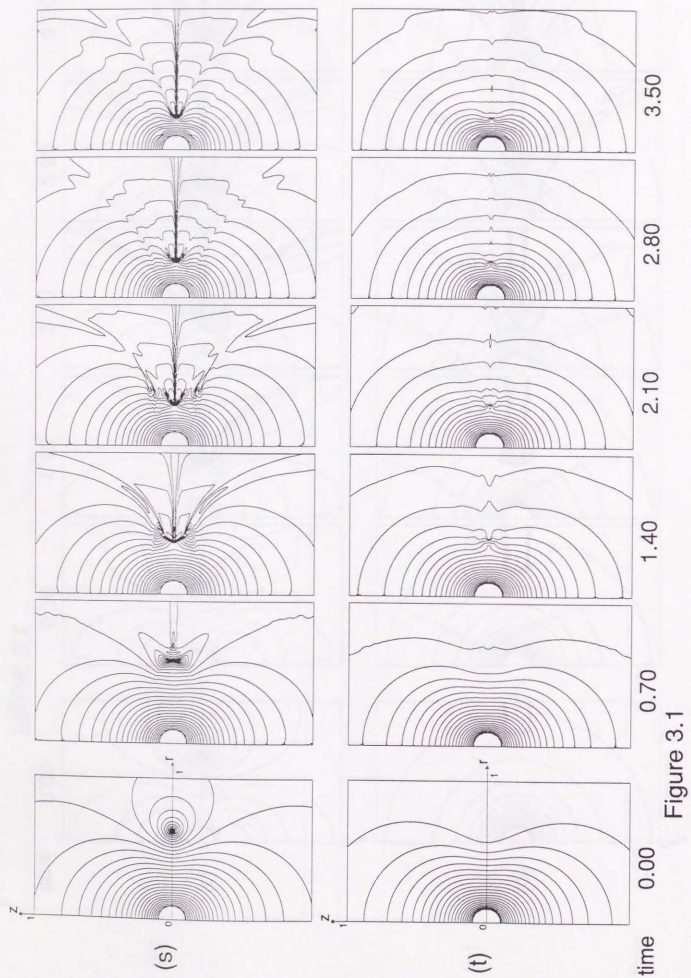


Figure 3.1

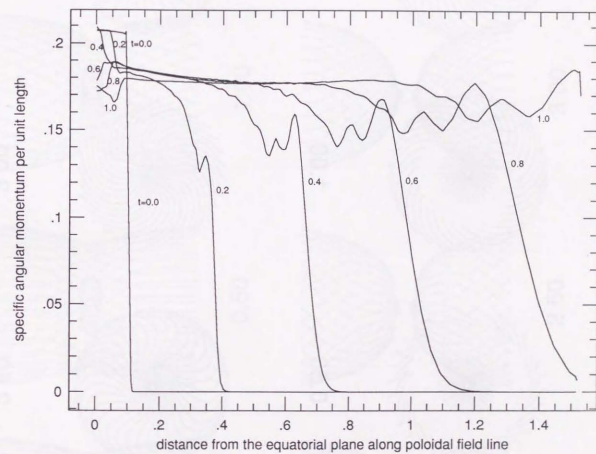


Figure 3.2

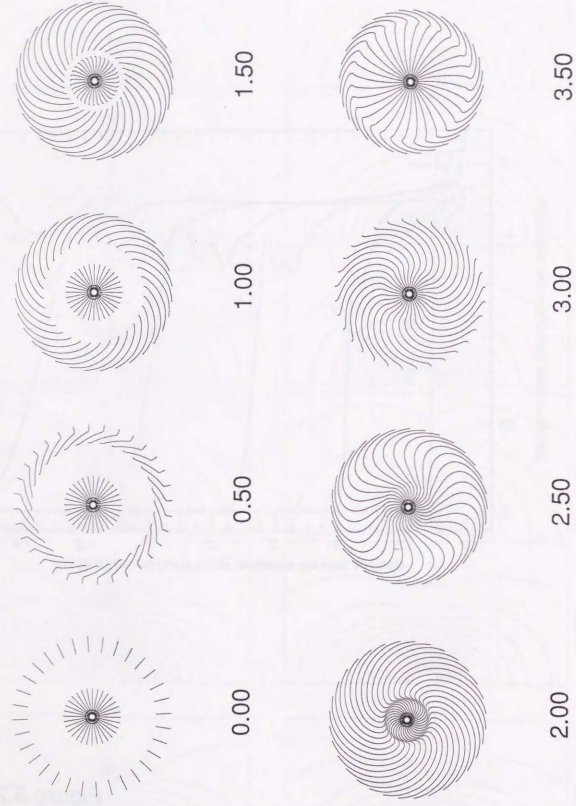


Figure 3.3(a)

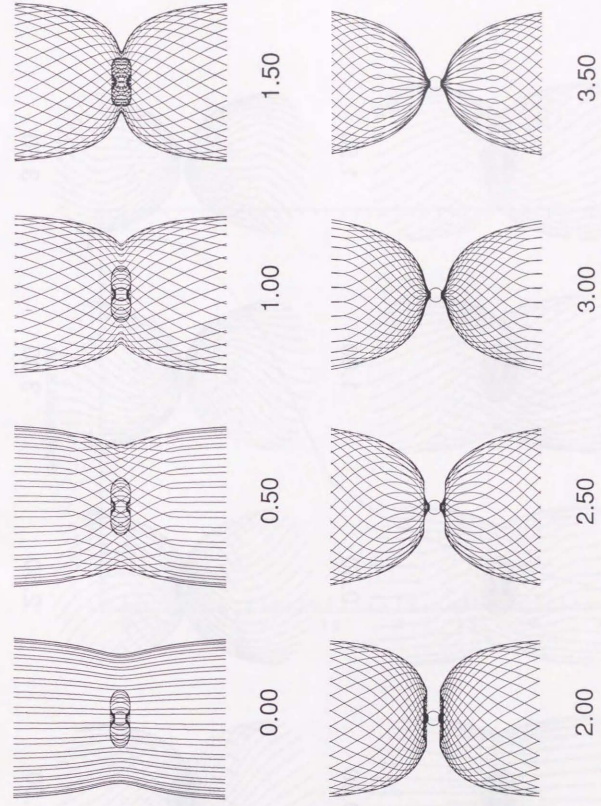


Figure 3.3(b)

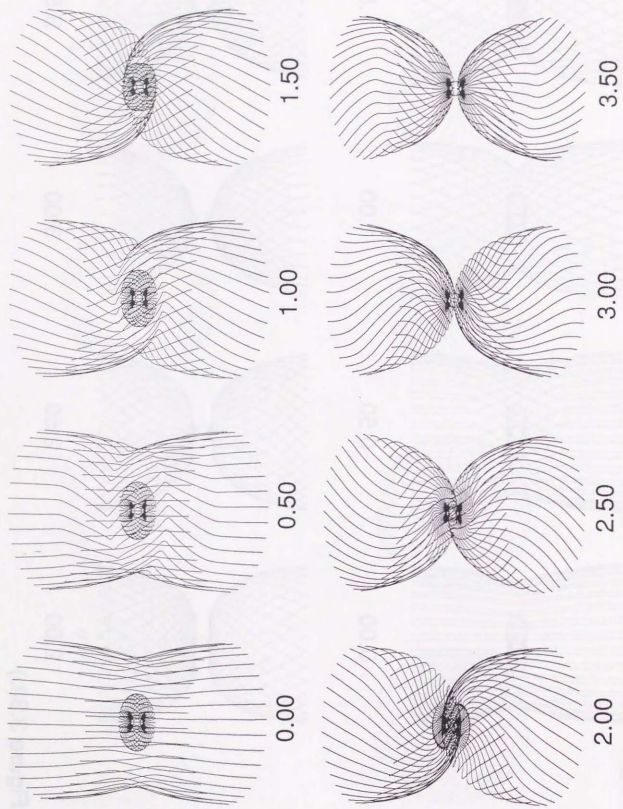


Figure 3.3(c)

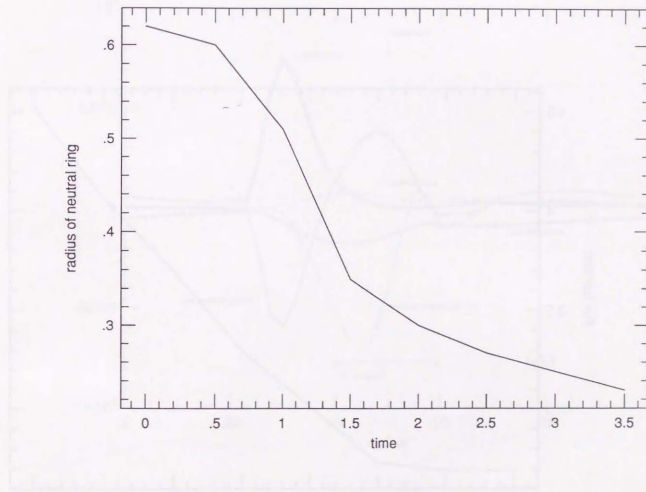


Figure 3.4(a)

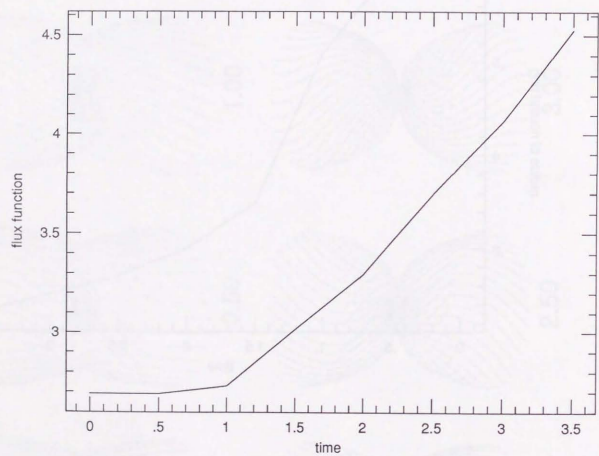


Figure 3.4(b)

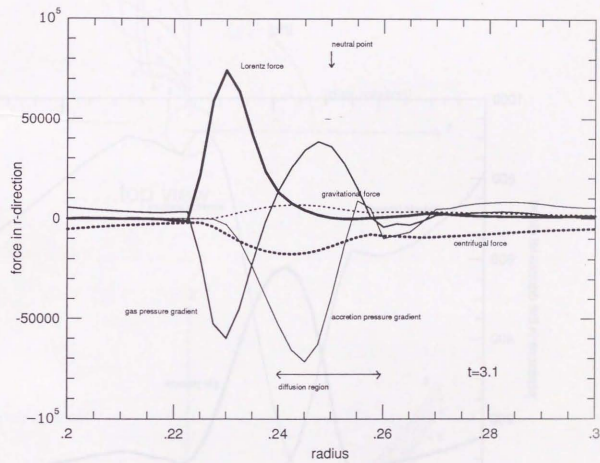


Figure 3.5(a)

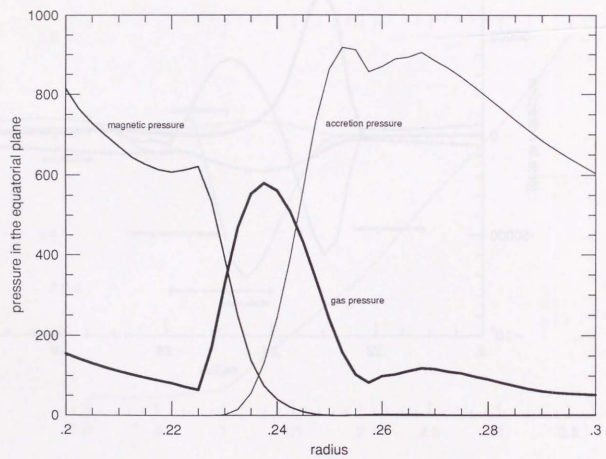
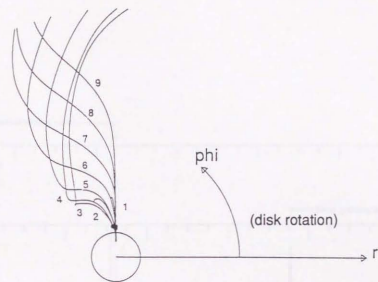
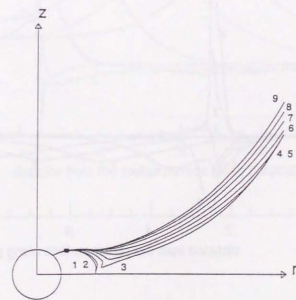


Figure 3.5(b)



top view



side view

Figure 3.6(a)

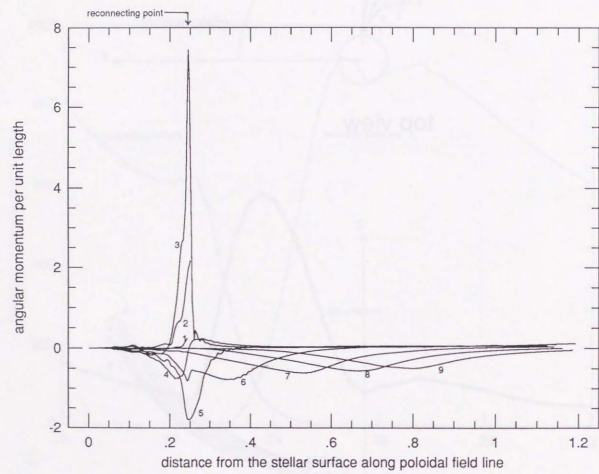


Figure 3.6(b)

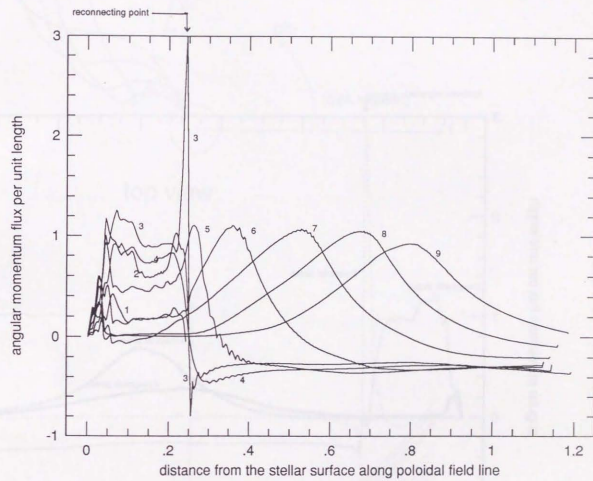


Figure 3.6(c)

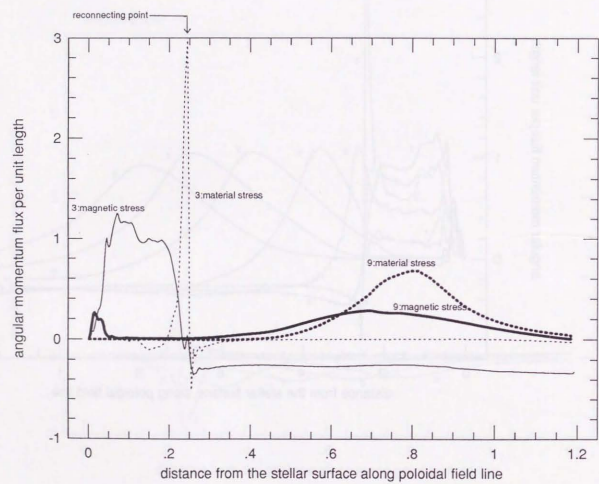


Figure 3.6(d)

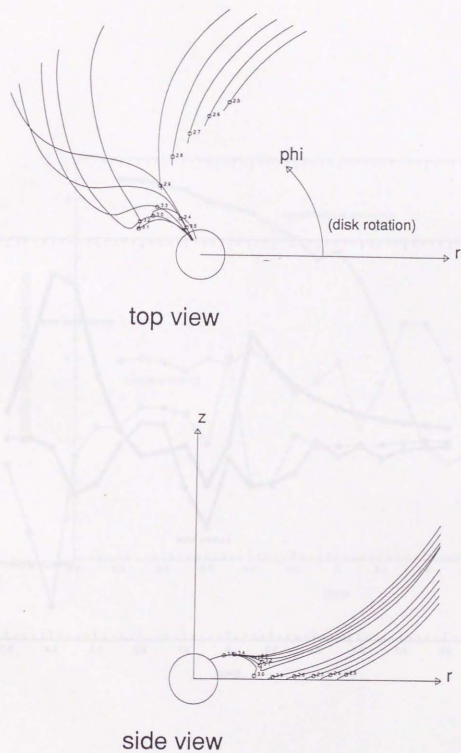


Figure 3.7(a)

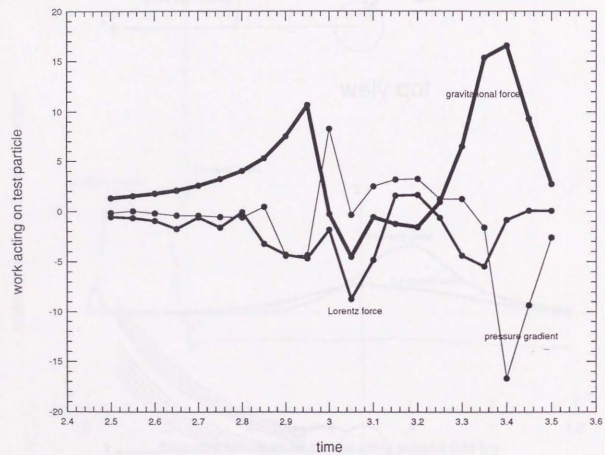


Figure 3.7(b)

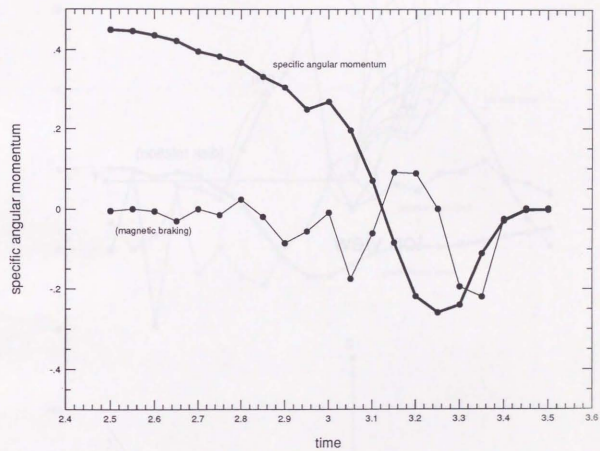
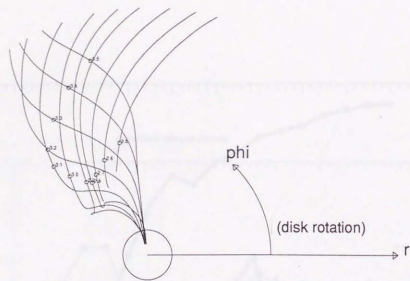
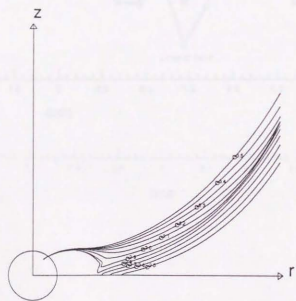


Figure 3.7(c)



top view



side view

Figure 3.8(a)

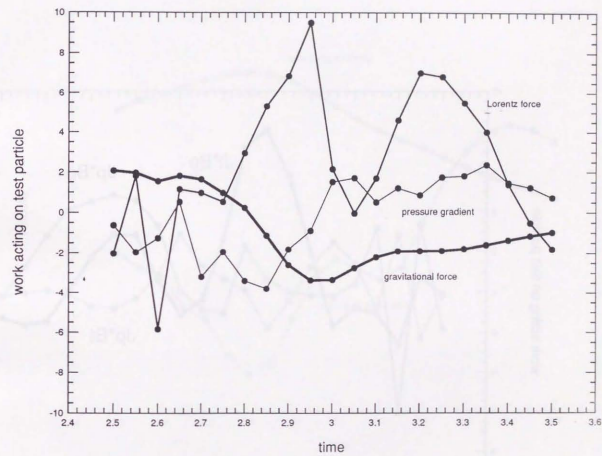


Figure 3.8(b)

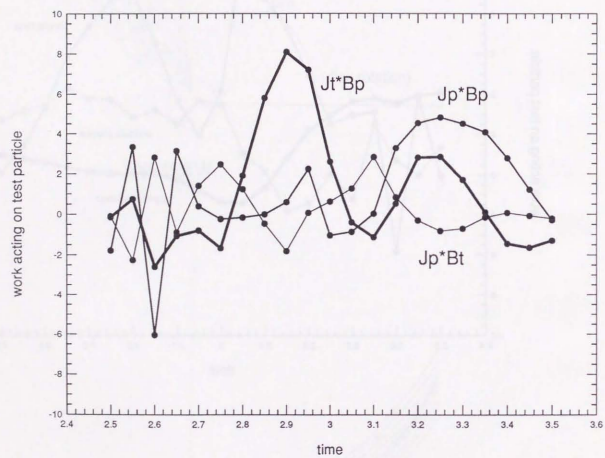


Figure 3.8(c)

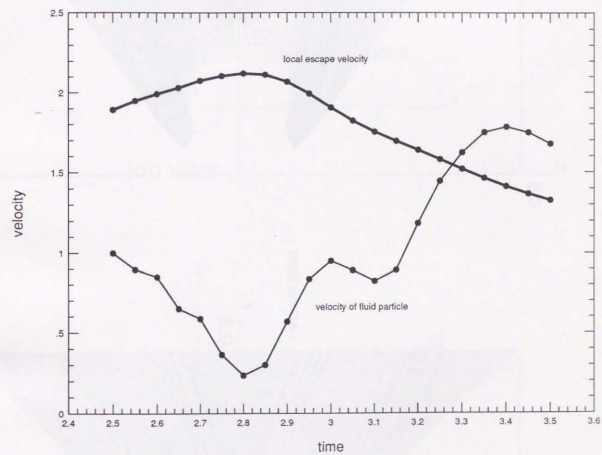


Figure 3.8(d)

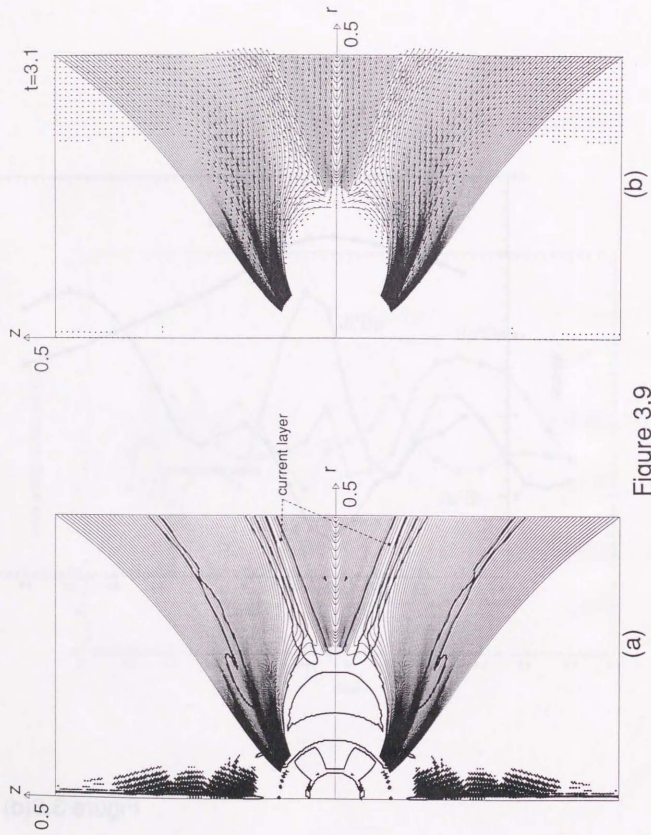


Figure 3.9

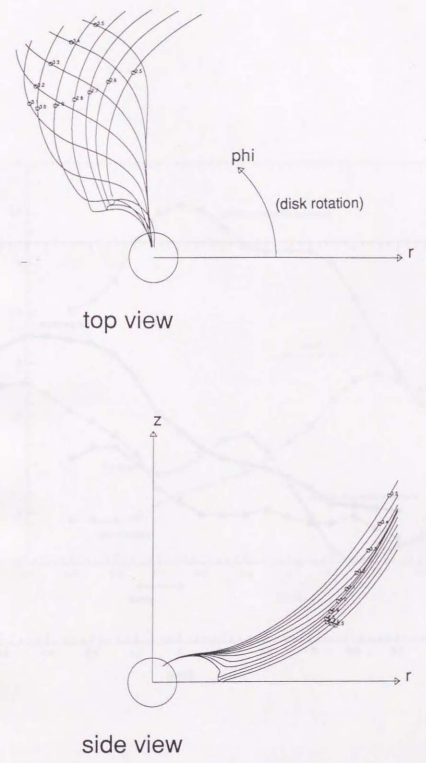


Figure 3.10(a)

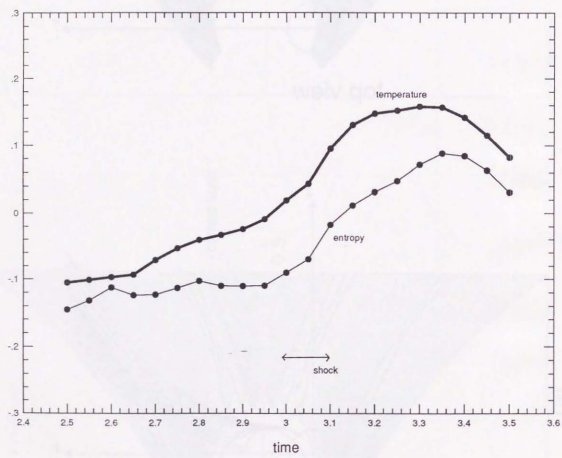


Figure 3.10(b)

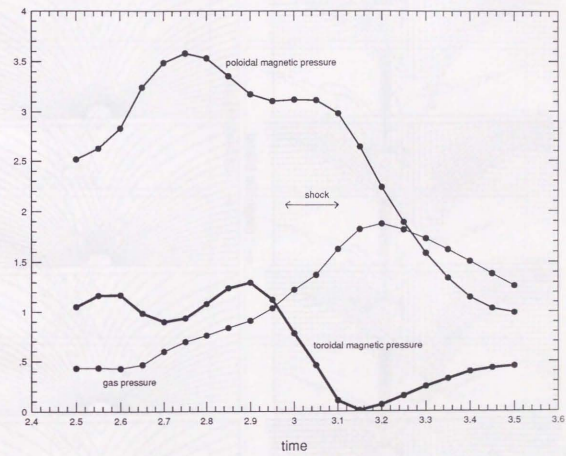


Figure 3.10(c)

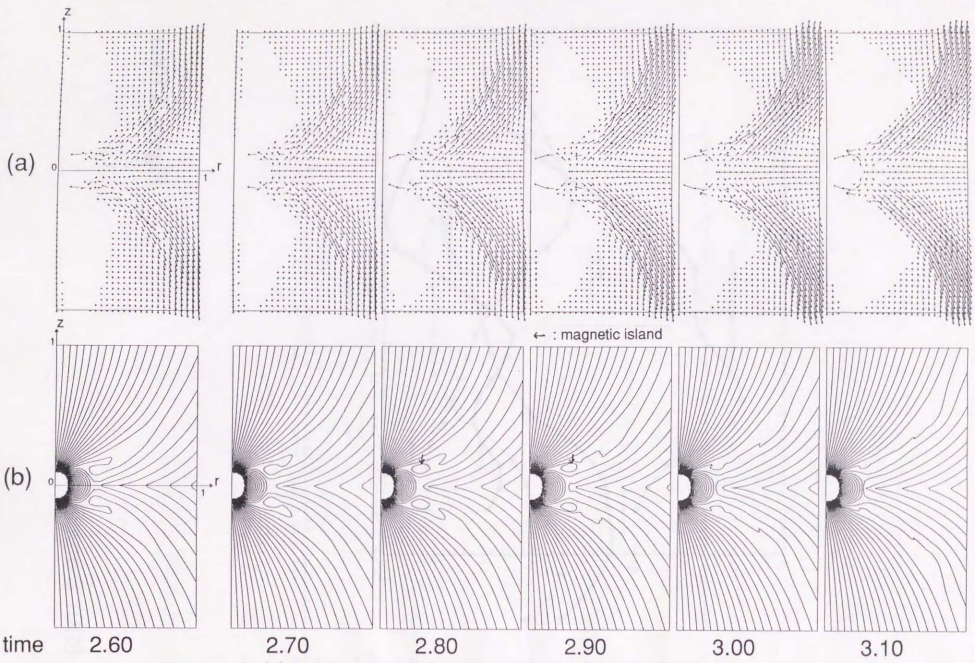


Figure 3.11

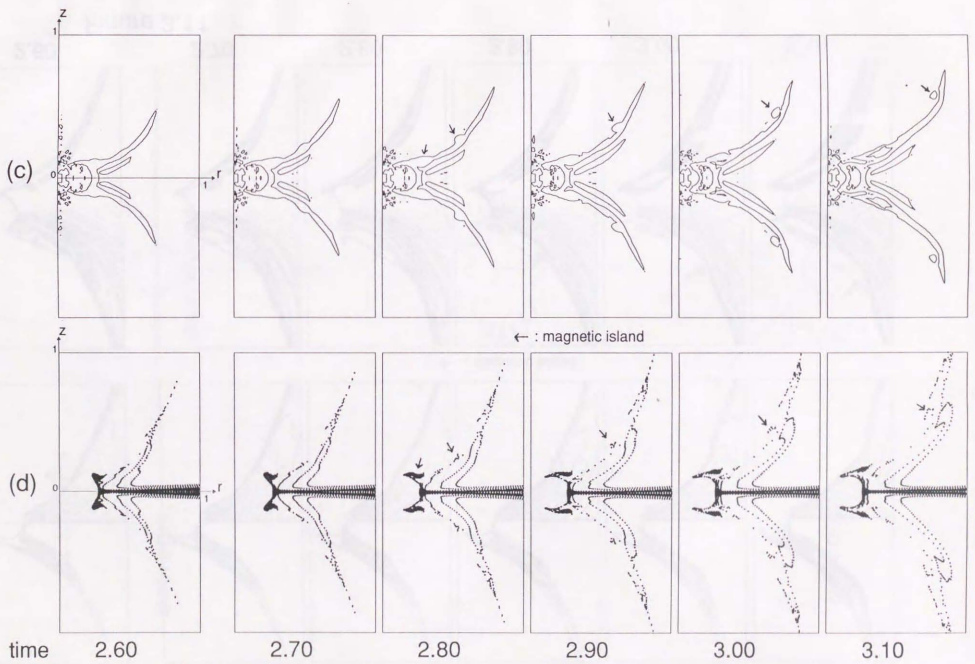


Figure 3.11

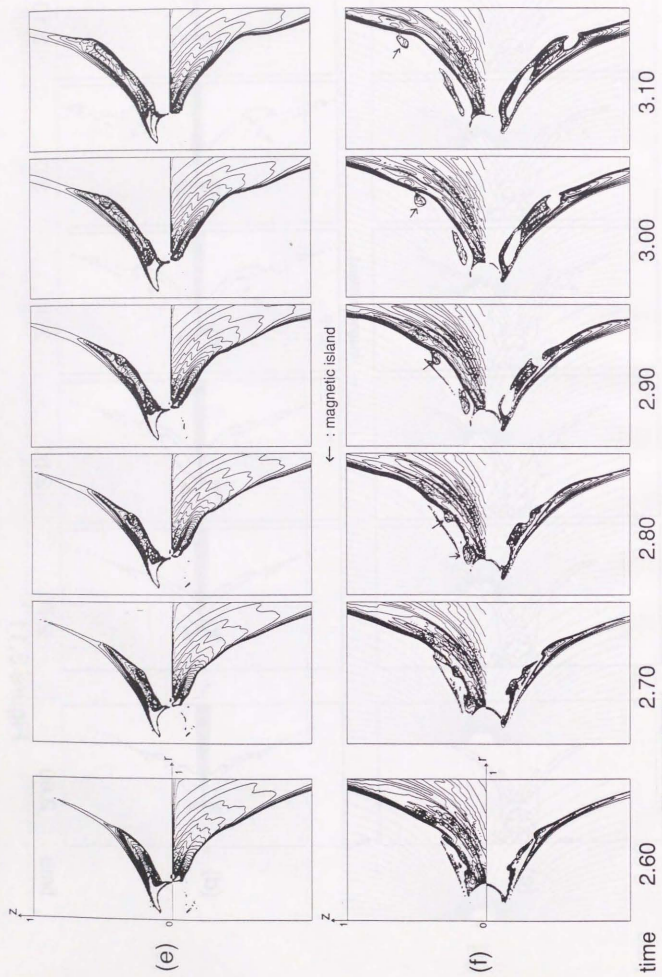


Figure 3.11

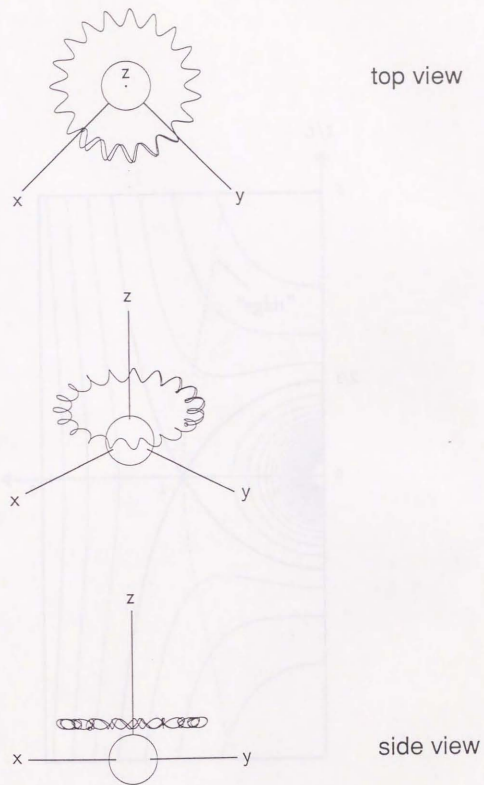


Figure 3.12

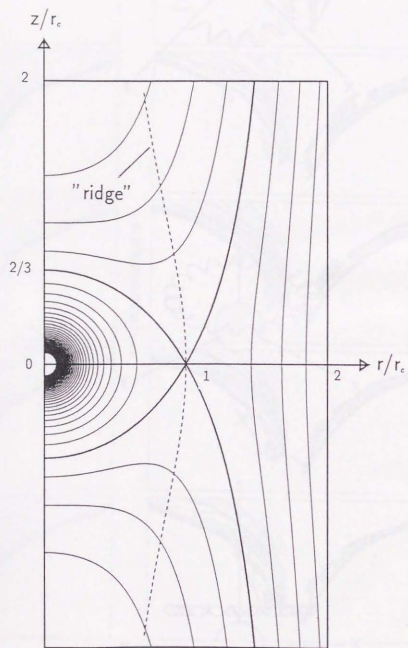


Figure 4.1

